3D PRINTING OF BIOMEDICAL DEVICES WITH SOFT AND BIOCOMPATIBLE ELASTOMERS

By
Runhan Tao

A thesis submitted to Johns Hopkins University in conformity with the requirements for the degree of Masters of Science

Baltimore, Maryland
May 2020

Abstract

Additive manufacturing (AM) which is commonly known as 3D printing is evolving quickly during the last decades. It has been utilized in various areas including biomedical applications, such as tissue engineering, therapeutic delivery, surgical planning and implant designs. The possibility to fabricate complex geometries allows us to solve many problems that cannot be done using traditional methods. In this thesis, we explored possible applications of 3D printing in biomedical engineering. The first application was using 3D printing to address challenges in treatments for congenital heart diseases (CHD). 1.35 million infants are born with CHD each year in the world, reconstruction of right ventricle–to–pulmonary artery (RVPA) continuity is an integral part of various surgical procedures commonly performed in neonates and young infants to treat CHD. However, these conduits need multiple open-chest replacement surgeries because the size of the conduits cannot grow as infants grow. We addressed the lack of growth potential of RV-PA conduits using novel 3D-printed conduits that can change their shape in response to the physiological changes during pediatric growth. We utilized thermoplastic polycarbonate-based polyurethane as a filament material in a fused filament fabrication printing process. We

characterized the material to determine the suitable printing parameters, then developed a customized bench-top fluidic set up to study the *in-vitro* functionalities of the 3D-printed conduits. The conduits can increase the effective diameters as the RV pressure increases during growth to accommodate increased blood flow rate. The second application was utilizing the same material to address the technique difficulties in vascular and microvascular anastomosis. Traditional suture method requires surgeons to have a long-time training before they can perform vascular anastomosis, and the surgeries usually last for hours, the sewing material may cause further damage to blood vessels after the surgery. To address these issues, we developed a 3D-printed device that can connect blood vessels together and allow a broader access of vascular and microvascular anastomosis by making the process simpler, faster, and safer. We believe that using 3D printing technology, we can provide new aspects in designing patient specific biomedical devices and develop experience of both patients and surgeons.

Primary Reader and Advisor: Sung Hoon Kang

Secondary Readers: David Gracias; Lewis Romer

Acknowledgments

I want to start by thanking my research advisor, Prof. Sung Hoon Kang, who has been a great mentor who has been generously provided me great research opportunities since my first year here at Johns Hopkins University. I would like to thank all the Kang Lab members and Dr. Ozan Erol, who has been both a great mentor and friend throughout the RV-PA research project. I would also like to thank Helen Xun from medicine school, who has been a great friend and partner throughout the sutureless coupler research project.

Thank you to Dr. Narutoshi Hibino, Dr. Lewis Romer, and Prof. David Gracias who contributed and provided great help to the RV-PA project. Especially, I would like to thank Dr. Romer and Prof. Gracias for being my thesis readers. Thank you to Dr. Justin Sacks who provided great opportunity and help to the sutureless coupler project. I would like to acknowledge Prof. Sharon Gerecht for her generousness in allowing me to use her lab equipment.

I would also like to thank all of my families especially my mother for supporting me to spend these wonderful two years and cheering me up whenever I am disappointed. Thank you to my friends here who accompanied me during these two years.

It has been an incredible two years at Hopkins, thank you to everyone who has helped me, and I wish all of my mentors and colleagues the best in your future.

Dedication

This thesis is dedicated to my parents, Ying Li and Lihe Tao, for their eternal love, trust and support. They are the reason I am the woman I am today.

Contents

List of Tables

List of Figures

1. Introduction

Additive manufacturing (commonly known as 3D-printing) technologies have been developed in the past few decades as a cost-effective, on-demand modality and has been used widely in biomedical engineering because of the capability to enable intricate and complex geometries[1] without expensive and time-consuming tooling. With 3D-printing, it is possible to design personalized devices and structures to address different needs and challenges in medical aspects. This thesis will provide studies on using 3D-printing technologies to produce medical devices for addressing two current challenges in biomedical engineering. One is the growth of children makes it impossible for them to use implant designed for a full-grown adult, the other one is the long learning curve, surgery time and high risks for surgeons to perform vascular and microvascular anastomosis. These studies will include the design, fabrication, and performance evaluation for both problems. In this chapter, basic concepts associated with the devices will be introduced.

1.1. Additive manufacturing and its applications

ISO/ASTM 52900 defines additive manufacturing (AM) as process of joining materials to make parts from 3D model data, usually layer upon layer[2]. AM is commonly known as 3D printing. Compared to conventional fabrication methods such as molding that are related to industrial mass production, AM enables faster design and manufacturing of customized objects to meet demands of specific applications. Commonly used AM techniques include fused filament fabrication (FFF), stereolithography (SLA), powder bed fusion, Direct ink writing.[3,4] Using these methods, a wide range of material can be utilized, including polymers, metals, bio-inks and ceramics.

We chose thermoplastic materials as our main component and the reasons for this choice are explained in chapter 2. Consequentially, fused filament fabrication was chosen as the 3D printing technology.

1.1.1. Fused Filament Fabrication

Fused filament fabrication (FFF) is one of the most widely used 3D printing technologies because of its simplicity. As shown in Figure 1, a thermoplastic filament is fed through an extruder which can melt the filament using heat. The nozzle moves along three axis (x-y-z) and put on the desired shape layer by layer, thus reproducing the designed model. There can be multiple nozzles in the FFF process. For example, one extrudes the building material while the other one extrudes supporting material which can support the over-hanging building structure and can be removed later, leaving the built model.

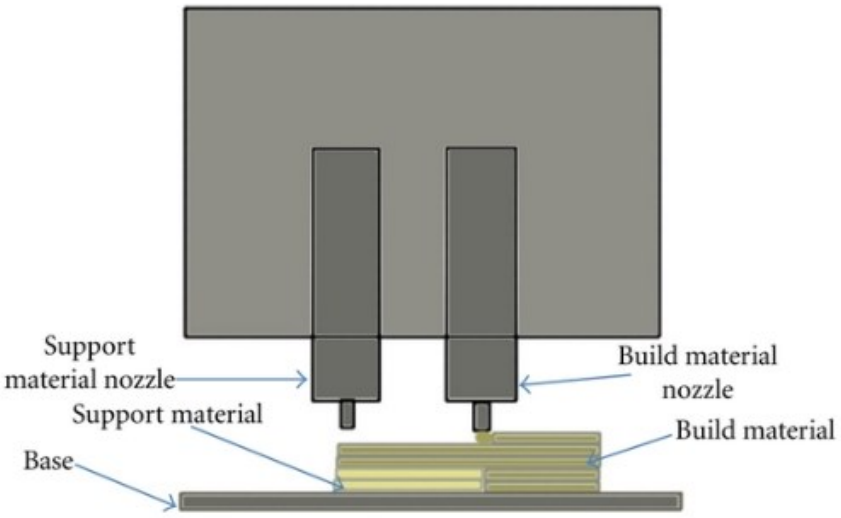

Figure 1: An illustration of fused filament fabrication process[i]

Materials commonly used in the FFF process are polycarbonate (PC), acrylonitrile butadiene styrene (ABS) and polylactic acid (PLA). The main advantages of FFF are 1) it is a relatively simple process, 2) generally no chemical post-processing required, and 3) most importantly, the materials that can be used in the process are versatile while they must be thermoplastics, which is

[i] Copyright © 2012 Kaufui V. Wong and Aldo Hernandez

also the reason that we chose FFF as our main fabrication method. However, it is also limited in the resolution (usually around 0.3mm) compared to other additive manufacturing process. The resolution of this method is not ideal for relatively small structures.

We used the FFF process to fabricate soft biomedical devices, more specifically, right ventricle-to-pulmonary artery (RV-PA) conduits and sutureless couplers. The usage and current development of the devices will be introduced in the following sections.

1.2. Applications of 3D printing

As AM techniques are developing rapidly, there has been an abundance of potential applications in biomedical engineering. In addition, 3D-printing is especially important for pediatric implants since many of the devices and implants that are needed are either based on adult applications or non-existent due to the high development costs and small markets.

1.2.1. 3D printing in biomedical engineering

3D printing technology has been used widely in biomedical engineering because of its ability to incorporate intricate complex structure into designs. These applications include:

- Tissue engineering

  3D printing technology is often used to print a customized scaffold to culture cells for in situ tissue regeneration. For example, Ma *et al.* 3D printed a biodegradable polymeric scaffold to enhance osteogenesis for bone regeneration[5] (Figure 2).

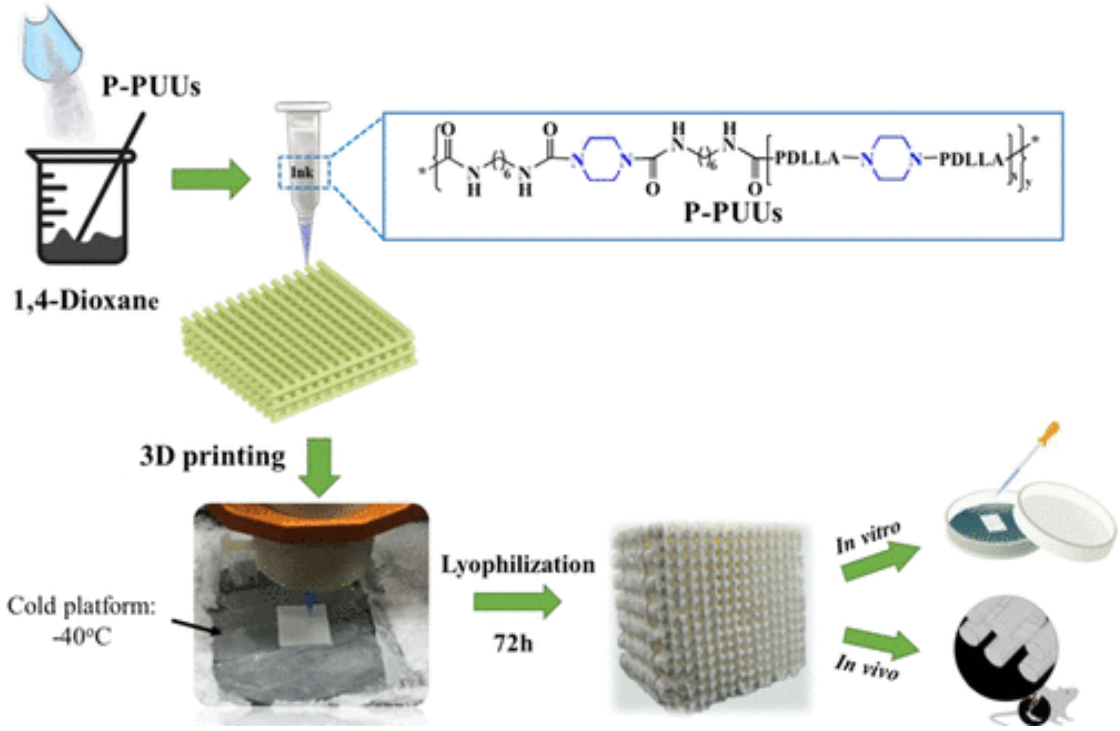

Figure 2: 3D printing technology utilized in bone regeneration.[ii]

- Therapeutic delivery

  Recently, 3D printing has gained traction in pharmaceutical manufacturing. Because a drug product's structure can affect drug release, complex 3D structures may create new possibilities for drug delivery[6]. Also, while conventional drug products are manufactured in a large quantity, 3D printing technology gives us more control of the structures and dosing of the drug for different patients.[7]

- Surgical planning and implant designs

  Some human structures are very complicated, and fractures may be difficult to fix. For example, the unique anatomy of the orbit makes it difficult and time consuming to fit

[ii] Reprinted with permission from Ma, Y.; Hu, N.; Liu, J.; Zhai, X.; Wu, M.; Hu, C.; Li, L.; Lai, Y.; Pan, H.; Lu, W. W.; et al. Three-Dimensional Printing of Biodegradable Piperazine-Based Polyurethane-Urea Scaffolds with Enhanced Osteogenesis for Bone Regeneration. ACS Appl. Mater. Interfaces 2019, 11 (9), 9415–9424. Copyright 2019 American Chemical Society.

and align implants after the fractures happened[8]. Using 3D printing, it is possible to plan the surgery (Figure 3a&b) and 3D print patient-specific implants before the surgery.

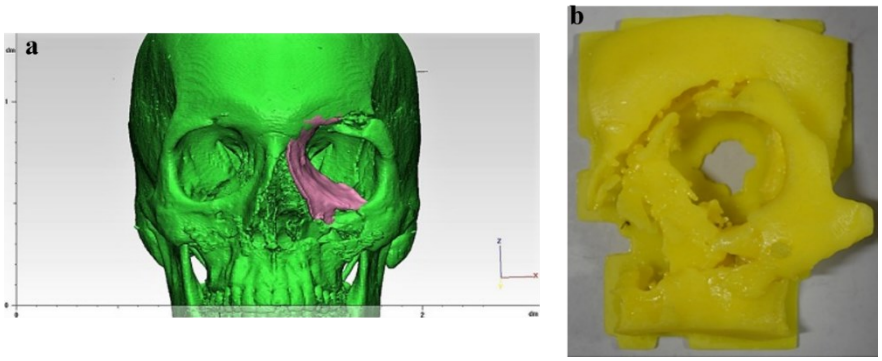

Figure 3: (a) Computer Assisted Designing of implant for 3D reconstruction of damaged part (pink in the picture). (b) Stereolithographic model showing fracture for treatment planning.[iii]

1.2.2. 3D printing for pediatric applications

Although 3D printing has been widely used in customized biomedical implants, pediatrics is an underserved market for implantable medical devices.[9] The most significantly challenge in pediatric biomedical implants is the need for devices to accommodate tissue growth.[9] Thus, producing 3D-printed devices that adapt to growing tissues is important for pediatric applications. For example, Morrison *et al.* reported a 3D printed patient-specific archetype device that allows radial expansion of the affected airway over the critical growth period while resisting external compression and intrinsic collapse to treat tracheobronchomalacia (Figure 4).[10] The implanted device will expand with the airway's growth due to the degradation of the material and decreased stiffness.

[iii] Reprinted from Journal of Oral Biology and Craniofacial Research, Volume 7, Vignesh et al., Three dimensional reconstruction of late post traumatic orbital wall defects by customized implants using CAD-CAM, 3D stereolithographic models: A case report, Pages 212-218, Copyright (2017), with permission from Elsevier

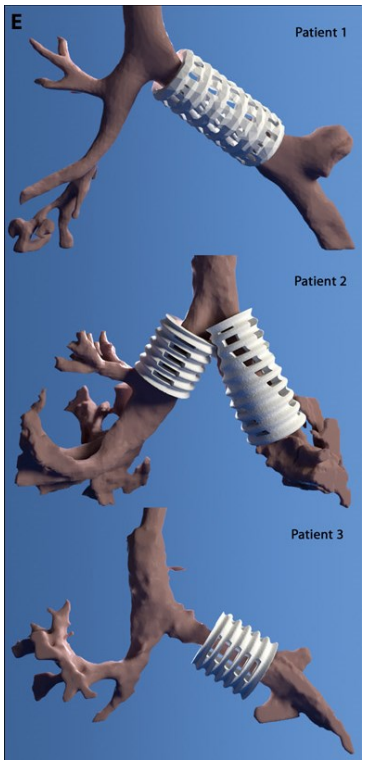

Figure 4: illustration of fit of patient-specific 3D printed PCL tracheobronchial splint over three different patients' airway.[iv]

Currently, the most commonly used method to make growth-accommodating implants is utilizing biodegradable materials,[11] which will limit the material choice, especially for 3D printing. Thus, there is rapid need to explore more options to make biomedical implants that can grow with human body.

1.2.3. 4D printing

Incorporated with multi-material prints which have the capability to transform over time, or a customized material system that can change from one shape to another, the concept of four-dimensional (4D) printing was developed recently. The technique that adds time as an additional

[iv] From Morrison, R. J.; Hollister, S. J.; Niedner, M. F.; Mahani, M. G.; Park, A. H.; Mehta, D. K.; Ohye, R. G.; Green, G. E. Mitigation of Tracheobronchomalacia with 3D-Printed Personalized Medical Devices in Pediatric Patients (Science Translational Medicine (2015) 7 (287er4)). Sci. Transl. Med. 2015, 7 (287), 1–12. Reprinted with permission from AAAS.

dimension to common 3D printing processes is defined as 4D printing. It usually needs external stimuli to trigger the change of the shape, such as light, heat and temperature. For example, Zarek *et al.* reported a 4D printed personalized tracheal stent which can deform into its temporary shape after printing, and be inserted in the body followed by deploying back into its permanent shape with a local increase in temperature (Figure 5).[12]

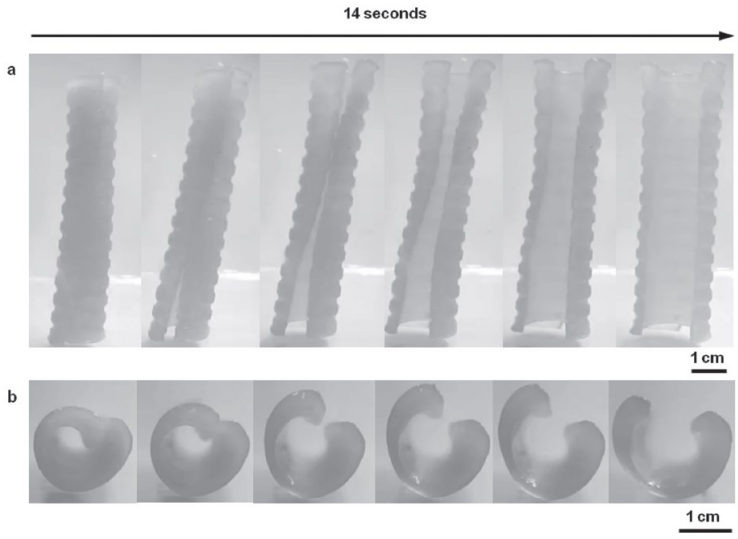

Figure 5: Photoseries of macroscopic shape memory behavior of a personalized airway stent. The images show the transition between the temporary state (for deployment) and the permanent shape (for performance)[v]

The stent was printed using shape-memory-polymer (SMP), which is a semicrystalline methacrylated poly-caprolactone (PCL) in this study. This device is also potential to accommodate growth, which is found much interest for pediatric applications. In this thesis, we will show a type of 4D printing biomedical device which can be used to treat congenital heart diseases.

1.3. Current state of art for RV-PA conduits

[v] Reprinted from Macromolecular Rapid Communications, Volume 38, M. Zarek et al., 4D Printing of Shape Memory-Based Personalized Endoluminal Medical Devices, Copyright (2016), with permission from John Wiley and sons.

Birth defects account for nearly 20% of infant deaths in the U.S.[13], and congenital heart disease (CHD) is the most common type of birth defect, for an overall prevalence of 81 per 10,000 births, worldwide, 1.35 million infants are born with CHD each year. Congenital heart disease impact cardiac embryogenesis both structurally and functionally. Common CHDs include pulmonary stenosis, tricuspid atresia, tetralogy of fallot and so on.[14,15] Tetralogy of fallot is one of the most common cyanotic congenital heart disease.[16] It includes 4 distinct morphologic abnormalities: a ventricular septal defect, rightward shifting of the aorta, right ventricular outflow obstruction, and right ventricular hypertrophy.[16] Right ventricle to pulmonary artery (RV-PA) conduits to reconstruct the RV-PA continuity are commonly used to treat CHDs (Figure 6).[17]

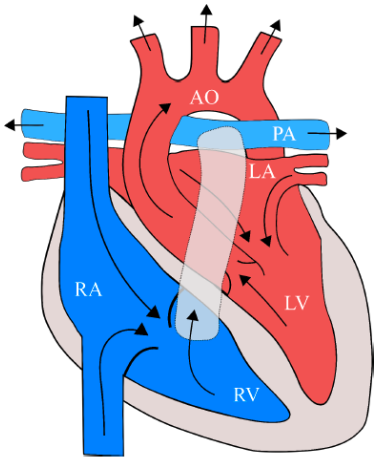

Figure 6: Reconstruction of the right ventricular outflow to the pulmonary arteries using an RV-PA conduit (the transparent tube)[vi]

Currently, commonly used conduit types include homografts, xenografts and polymeric implants.[18] However, the sizes of these conduits are fixed so that most of these implants eventually require replacement after years. The conduit durability is usually 5-6 years in younger stage[19–21] because the size of the conduit needs to be small due to the limited space in neonate's chest. Hence,

[vi] Reprinted from Ozan Erol et al. 3D-Printed Shape-Changing Cardiovascular Conduits to Accommodate Growth of Pediatric Patients, in preparation.

the dominant issue in the patients' long-term course becomes subsequent open-chest surgeries during their lifetimes.

1.3.1. Engineering of current conduits

In order to overcome the limitations of static conduits, several studies have tried to engineer the current cardiovascular conduits used for CHDs in order to give growth potential. The engineered conduits can be divided into two categories: vascular tissue engineering[22–25] and synthetic implant[26–28].

Vascular tissue engineering is governed by the tissue engineering triad, which consists of the scaffold, cells and signals. Tissue engineered vascular grafts (TEVG) are based on either decellularized extracellular matrix (ECM)[25] or biodegradable scaffolds.[22–24] The cells seeded in the scaffold are expected to proliferate and differentiate after implantation, and after the scaffolds degraded, the differentiated cells are expected to form neovessels that can repair, remodel, and even grow with the patient (Figure 7).[29] It has been proved that tissue-engineered cardiovascular substitutes had evidence of growth in lambs,[23] and in the clinical trial performed in Japan showed that the TEVG grown with time without thrombosis, stenosis or obstruction.[30] However, the cellular and molecular mechanisms of TEVG neotissue formation in the human trial remained unidentified and unexplained which have large influence on the choice of scaffold and seeding cells,[31] and further studies are needed.

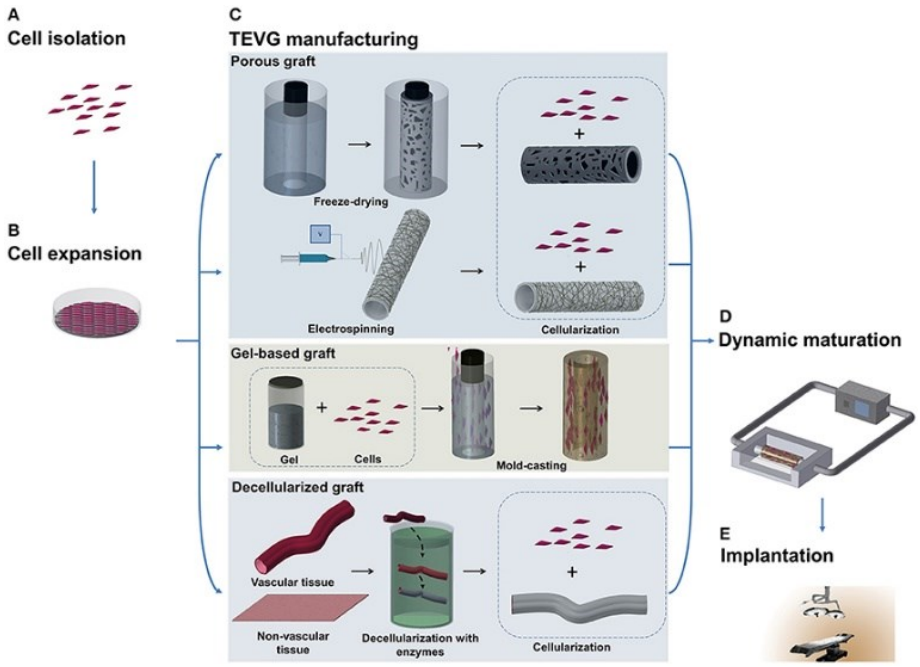

Figure 7: Schematic illustration of TEVG manufacturing process. (A, B) Cells are isolated from tissues obtained from patients and expanded in vitro. (C) Fabrication techniques. (D) The TEVG undergoes cellularization with the expanded cells before moving to dynamic conditioning. (E) The manufactured TEVF is implanted into the patient.[vii]

Synthetic conduits are made of biocompatible materials, such as expanded polytetrafluoroethylene (ePTFE) are alternatives to homografts and showed growth ability, however it has been challenging due to limited fabrication ability to make small conduits that can fit infants.[27] Other techniques that have been use to delay the need for reoperation including different kinds of cardiovascular stents (balloon expandable[32] or self-expandable[33]), however, the fracture of cardiovascular stents remains a large concern[34] and there have not been any Food and Drug Authority (FDA) approved intravascular stents for use in CHD.[35]

1.3.2. Shape-changing biomedical devices

Recently the shape-changing biomedical devices have become an active and important research area. Stimuli-responsive materials that are capable of controlled shape transformations

[vii] © 2018 Carrabba and Madeddu

have been choices for making shape-changing biomedical devices and other biomedical applications.[36,37] The shape-changing mechanism is realized by external stimulus such as heat, light, and PH.[38,39] It has been reported that stents, which are made of shape-memory polymer (SMP), can maintain shape storage at room temperature. When stents are implanted into human body, the body temperature can fully activate them, providing a new way to treat cardiovascular diseases (Figure 8).[40] In this study, SMP can be transferred into a soft rubbery state after heating above its glass transition temperature (T_g). The polymer is then deformed and cooled under constraint to set the material into a temporary packaged state. Shape-memory activation occurs when the polymer is reheated to T_g and returns to its original permanent shape. By utilizing this mechanism, the SMP stent is heated to deform before it is inserted into a glass tube and when the temperature is cooled down to body temperature, the stent goes back to its original shape and can act as a stent (Figure 8).

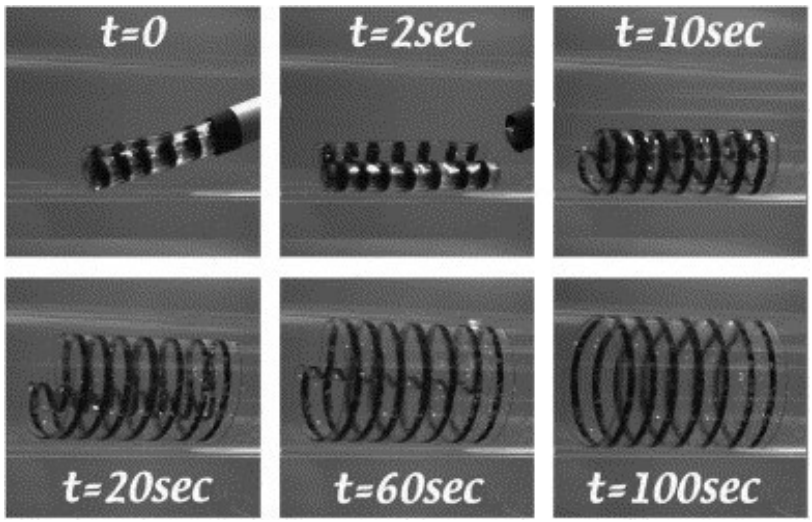

Figure 8: Recovery of a SMP stent with T_g=52 °C delivered via a catheter into a glass tube containing body temperature water at 37 °C. Black rings were drawn to facilitate deployment visualization.[viii]

[viii] Reprinted from Biomaterials, Vol 28, Yakacki et al., Unconstrained recovery characterization of shape-memory polymer networks for cardiovascular applications, Pages 2255-2263, Copyright (2007), with permission from Elsevier.

Although the shape-changing biomedical devices have shown their great potential in tissue engineering, drug delivery, wound healing, microsurgeries[41–43], they need continuous stimulations to remain in the changed shapes, which makes them unsuitable for long term biomedical devices that need progressive changes. There is currently no good solution to address the challenge of growth potential in RV-PA conduits.

1.4. Current state of art for sutureless couplers

Vascular and microvascular anastomosis is a procedure commonly performed by a broad range of surgeons including vascular, transplant and plastic surgeons. The anastomosis focuses on connecting blood vessels (arteries and veins) to restore blood flow. Reconstructing vessels with an outer diameter between 1mm and 3mm is considered as microvascular anastomosis.[44] The common procedure to connect the two ends of vessels together requires precise placement of sutures through the blood vessel wall (Figure 9) and it has been a great challenge for surgeons for over 100 years.[45] One of the big challenges is that surgeons need to be trained for years to be proficient in doing anastomosis, especially for small vessels (diameter <3.0 mm), which results in a short supply of skilled surgeons for highly demanded procedures.[45,46] On the other hand, even with skilled surgeons, the traditional method can lead to long-term failure from intimal hyperplasia and foreign-body reaction to the suture material.[47] The procedure is also resource intensive, often requiring high grade surgical microscopes, and specially trained staff to handle microsurgery equipment.

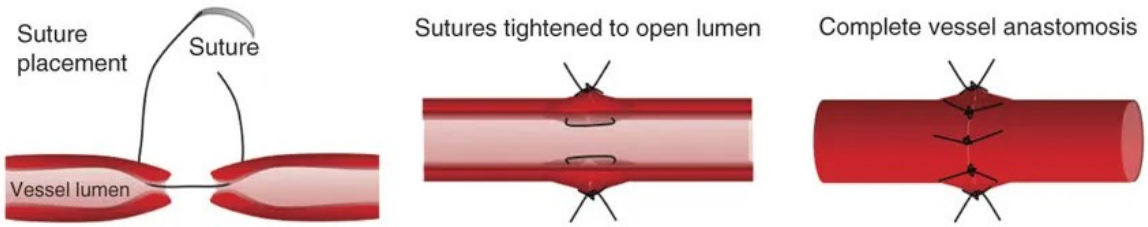

Figure 9: Diagram of the traditional vascular anastomosis procedure[ix]

A number of methods have been developed to overcome the technical difficulties of sutures, including using vascular connectors[48], shape-memory alloy stent[49] and poloxamer gels[50]. As shown in Figure 10, vascular connectors are composed with 3 parts, including the inner tube to support blood vessels, two outer rings to secure the position of the connectors on the blood vessels. Shape-memory alloy stent expands after deploying in the blood vessels while it needs glue to stabilize the connecting spots. The poloxamer gels are heated to be solid and act as temporary stent, when the adhesive solution is solidified outside the junction site, the poloxamer gels will melt at body temperature.

However, all these methods still need several steps to fully deploy the devices, they either need to wait for the temperature changes or have several pieces to finish the procedure. Also, they haven't been tested in large animal models to show their efficacy when compared with traditional methods. Consequently, there is a need to produce a robust, simplified, and faster method for vascular and microvascular anastomosis with comparable surgical outcomes.

[ix] Reprinted by permission from SPRINGER NATURE, Vascular anastomosis using controlled phase transitions in poloxamer gels, Chang et al. © 2011

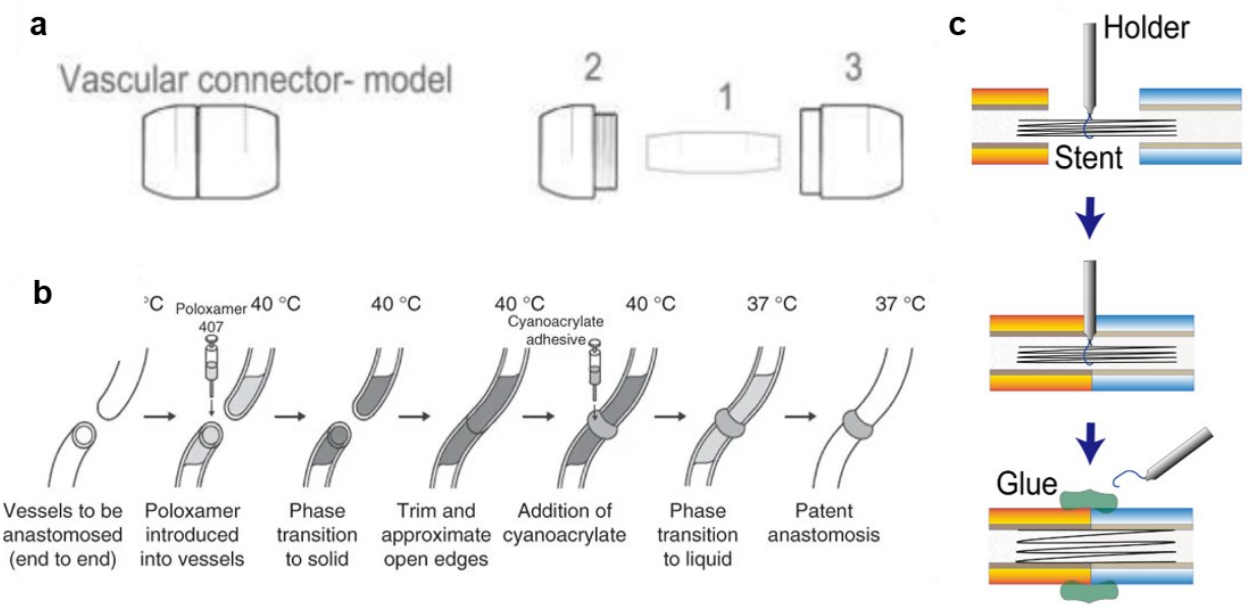

Figure 10: Schematic representations of different approaches to realize sutureless microvascular anastomosis (a) The new vascular connector: 1. The inner tube with conical ends, 2. Male ring, 3. Female ring.[x] (b) The Microstent system to perform sutureless microvascular anastomosis.[xi] (c) The poloxamer nanogel formulation as a temporary intraluminal stent to facilitate a stable, sutureless end-to-end microvascular anastomosis.[xii]

1.5. Thesis outline

To address aforementioned issues, we investigated 3D-printed cardiovascular conduits that can change their shapes in response to physiological changes to address the limitation in growth potential in current methods. The conduits were designed to have folds that can unfold with the physiological changes and increase their diameters. We also 3D-printed one-piece sutureless couplers that can hold two separate blood vessels together without suture to address the limitations associated with technical difficulties of anastomosis. The couplers had anchors on two ends that can hold the blood vessels and stay in site.

---

[x] © 2014, Springer Nature
[xi] Reprinted by permission from SPRINGER NATURE, Vascular anastomosis using controlled phase transitions in poloxamer gels, Chang et al. © 2011
[xii] © 2017 Saegusa et al.

The conduits and couplers were fabricated using fused filament fabrication (FFF)-based 3D printing with a biocompatible thermoplastic elastomer. The growing ability of the 3D-printed conduits were measured in our *in-vitro* flow test setup that can generate pulsatile flow and mimic pulmonary circulation at different ages. The feasibility of the 3D-printed sutureless couplers were tested using pig blood vessels and the preliminary ability of the couplers to sustain flow was measured.

This thesis is structured as follows:

- Chapter 2 will describe the material that we used in the studies to 3D print RV-PA conduits and sutureless couplers. We evaluated the thermal properties of the material and the printability of the material. These tests were conducted to define the printing parameters of this material using FFF method.
- Chapter 3 will describe the design details of RV-PA conduits and sutureless couplers including the inspiration and adjustable parameters in the designs.
- Chapter 4 will describe a customized *in-vitro* blood-flow simulation test set up which was used to evaluate the conduit's performance. A number of tests including the calibration of the test units and the performance of the conduits are described.
- Chapter 5 will describe the *ex-vivo* tests to explore the feasibility of the 3D-printed sutureless couplers. The preliminary data of the ability to sustain flow in the connected blood vessels are also described.
- Chapter 6 will discuss conclusions and future directions for the studies.

2. 3D-printing soft biocompatible materials

The printing material that we use should be soft and biocompatible so that it can accommodate with surrounding tissues without causing any compliance mismatches between the implants and tissues, as well as safe for human tissues so that there will not be infections after implantation. Considering these conditions, we think a polymer, especially soft elastomer is the best choice for our applications. Polymers are commonly used for vascular grafts.[29,51] They can provide high fatigue life and high compliance,[52] which are two properties that are important for cardiovascular applications. Polymers are also highly processable, which makes them suitable for a wide variety of manufacturing approaches. Thus, we chose the commercially available thermoplastic polycarbonate-based polyurethane silicone (Chronosil, AdvanceSource Biomaterials Corp) as the material for our studies. In the following sections, rationale to use this material and several tests to determine the printing parameters will be described.

2.1. Thermoplastic polycarbonate-based polyurethane silicone

TPU is a block copolymer that has hard segments and soft segments (Figure 11). The hard segments are joined to the soft segment through urethane linkage.[53] The regional heterogeneity and hard-soft interactions provide TPU both high elasticity and thermoplastic nature.[53]

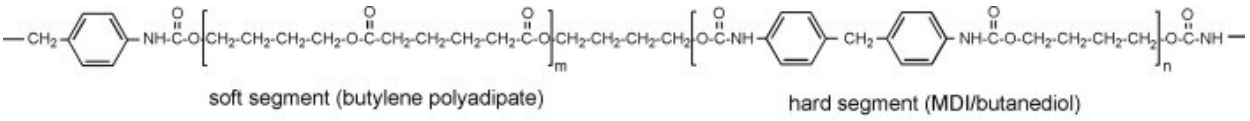

Figure 11: Structure of a thermoplastic polyurethane elastomer E685[xiii]

[xiii] Reprinted from European Polymer Journal, Vol 48, Françoise Fenouillot et al. Coarsening of nanodomains by reorganization of polysiloxane segments at high temperature in polyurethane/α,ω-aminopropyl polydimethylsiloxane blends, Pages 284-295., Copyright (2012), with permission from Elsevier.

These properties make TPU an ideal material for the FFF process. Thermoplastic polycarbonate-based polyurethane silicone (Chronosil) is a class of thermoplastic polyurethane mad by co-polymerizing silicone with polycarbonate-urethane. Pure silicones lack the mechanical integrity that are usually required for medical devices, but with polycarbonate-urethane co-polymerized, the mechanical properties are improved while the thermoplastic properties will not change. Recently, a study utilizing the similar copolymer thermoplastic silicone-polycarbonate-urethane (TSPCU) to 3D print heart valve ring showed great promise of using this material for medical applications.[54] The TSPCU that we used in this study was Chronosil 80A-5%-Q (AdvanceSource Biomaterials Corp) which was purchased in pellet form, 5% indicating silicone content by weight and 80A indicating shore hardness. We explored the thermal properties to determine the suitable printing parameters. The detailed printing process will be discussed in the following sections.

2.2. Characterization of thermal properties for 3D printing

As described in the introduction, FFF-based 3D printing melts the thermoplastic material, extrudes through a nozzle and deposits onto a substrate. Hence, the thermal and temperature-dependent rheological properties were characterized to guide the printing process. Micro-CT was used to visualize the printing quality of samples printed using different printing parameters.

2.2.1. Differential scanning calorimetry and thermogravimetric analysis

Differential scanning calorimetry (DSC) and thermogravimetric analysis (TGA) were conducted to characterize the thermal properties of Chronosil. DSC is a technique that measures the difference in the amount of heat required to increase the temperature of a sample and reference, while TGA can determine the thermal stability of our material. Both pellet and filament samples had a glass transition temperature around -30 ℃, which is common with polycarbonate-urethane

(PCU) based polymers. The first-order transition at around 160 ℃ corresponds to a typical melting temperature of PCUs (Figure 12a)[53]. Significant weight loss was observed at temperatures higher than 300 ℃ (Figure 12b)[53]. The start of the thermal degradation of Chronosil is important as the material is melted and extruded during FFF process.

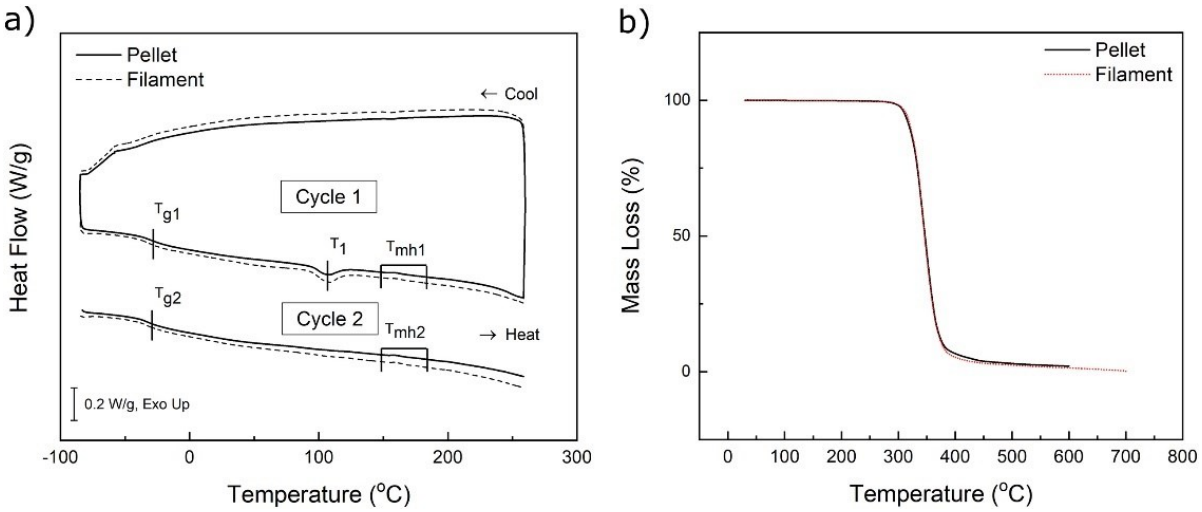

Figure 12: (a) Representative DSC curves for Chronosil pellet and filament. An exothermic reaction is in the upward direction. The temperature at which the sample goes through enthalpic relaxation is marked as T1 and melting endotherm region is marked as T_{mh} (b) A representative TGA thermogram of Chronosil pellet and filament.[xiv]

2.2.2. Rheology properties of Chronosil

The temperature-dependent rheological properties of Chronosil needs to be conducted to guide the printing process. Rheology studies the flow of matter and can measure the complex viscosity. The viscosity of the material in around the certain angular frequency at different temperatures can guide us to choose the suitable printing temperature.

[xiv] Reprinted from Journal of the Mechanical Behavior of Biomedical Materials, Vol 104, Bachtiar et al., 3D printing and characterization of a soft and biostable elastomer with high flexibility and strength for biomedical applications, Copyright (2020), with permission from Elsevier.

The filaments were cut into several segments (~ 2cm, Figure 13a) to fit the rotational rheometer (MCR-9, Anton-Paar Instruments). We used a parallel plate-to-plate setup capable of varying environment temperature with a 1mm gap to place the filament segments (Figure 13b).

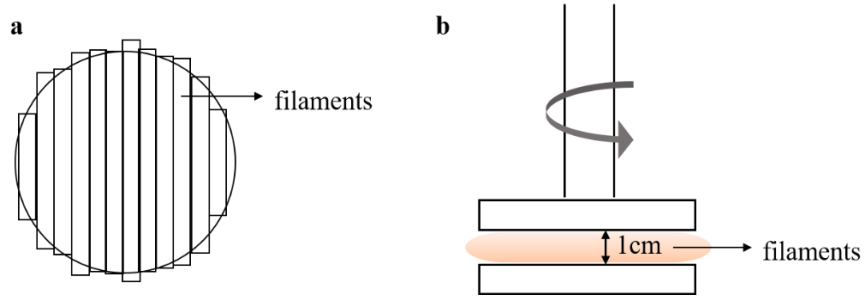

Figure 13: (a) Schematic illustration of upper view of cut filament segments lining on the plate. (b) Schematic illustration of rheometer set up.

The measurements were conducted at temperatures between 160 ℃ and 260 ℃ with 20 ℃ increments. The lower limit of the temperature was chosen as 160 ℃ , which is suggested as the melting temperature from DSC results, and the upper limit of the temperature was chosen as 260 ℃ as Chronosil starts exhibiting significant thermal degradation above this temperature.[53] For each temperature level, the frequency sweep was from 1 rad/s to 100 rad/s as the highest frequency sweep that the rheometer can reach is 100 rad/s, and the shear strain was 0.5% constantly.

The complex viscosity of the filaments was measured at different temperatures as a function of angular frequency (Figure 14). The viscosity of Chronosil filaments decreased as the temperature increased.

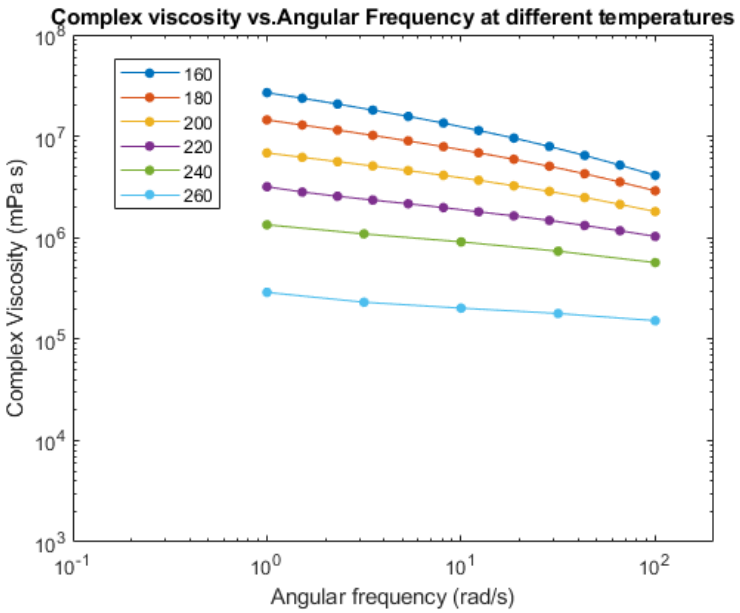

Figure 14: Theology properties of Chronosil at different temperatures

The range of angular frequencies that Chronosil experiences during printing with printing speeds ranging from 1mm/s to 50mm/s with a 0.35mm nozzle diameter was calculated to range between 20 s^{-1} to 1100 s^{-1} in the study by Bachtiar *et al.*[53] Because the oscillatory shear rheometer cannot reach angular frequencies above 100 rad/s, temperature-time superposition (TTS) was used to estimate the complex viscosity[55] at different temperatures (Figure 15). The viscosity of chronosil melts decreased as the temperature increased, suggesting shear-thinning properties that are commonly seen in polymer melts.

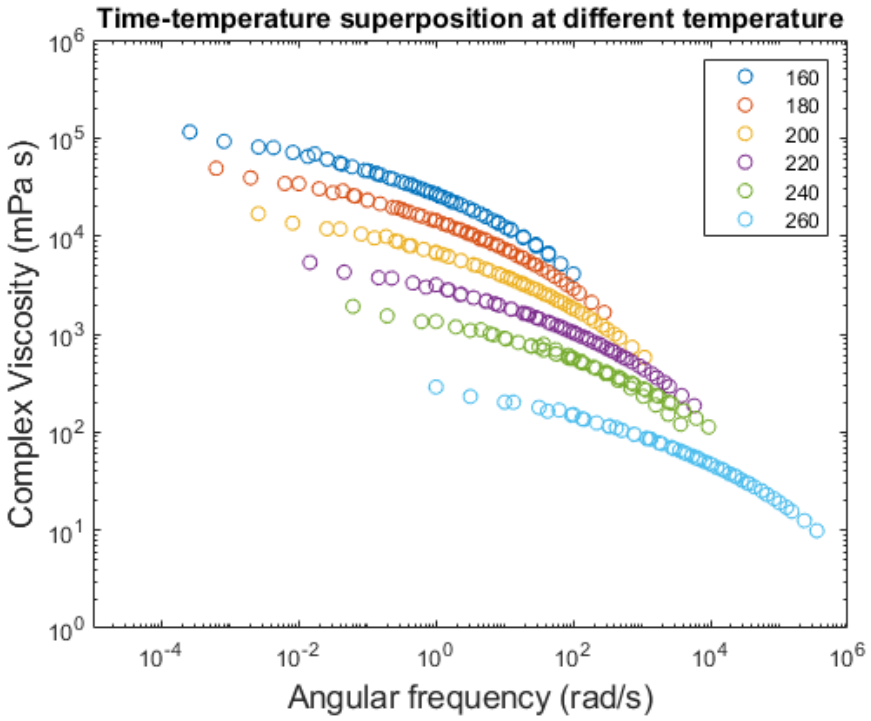

Figure 15: Rheological properties of Chronosil filaments determined by TTS at different temperatures

2.2.3. Determination of optimal printing parameters

To determine optimal printing parameters, single-walled hollow cubes were 3D printed under different temperatures, printing speed and layer height, and then scanned using micro-CT for reconstructing 3D models. Figure 16 shows the 2D cross-sections obtained from micro-CT scans under different printing conditions.[53] Distinct differences in porosity and geometric dimensions were observed. The green border indicates the best printing parameters that we chose, as it shows lowest porosity and finest geometric dimension among all the printed samples. The green border in the figure indicates the printing parameter that we chose, with the lowest porosity and finest geometric dimension among all the printed samples.

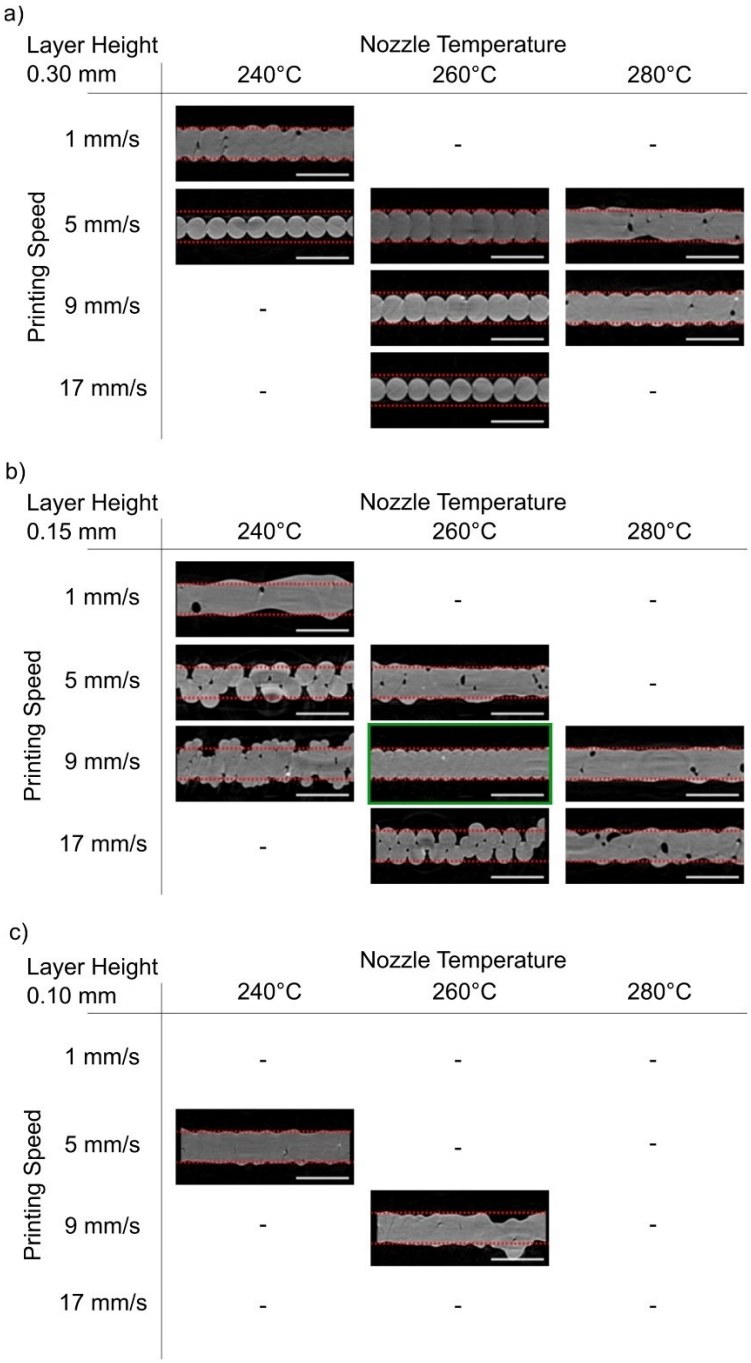

Figure 16: 2D cross-section images of 3D-printed objects using different printing parameters. a) Objects with 0.3 mm layer height, b) objects with 0.15 mm layer height, c) objects with 0.10 mm layer height. (Red dotted borders indicate the intended structure thickness of 0.35 mm. Scale bar represents 0.5 mm. The absence of any image indicates that objects were not printable).[xv]

[xv] Reprinted from Journal of the Mechanical Behavior of Biomedical Materials, Vol 104, Bachtiar et al., 3D printing and characterization of a soft and biostable elastomer with high flexibility and strength for biomedical applications, Copyright (2020), with permission from Elsevier.

2.3. Details of 3D printing

The architecture design of the conduits and couplers were generated using SOLIDWORKS™ 3D computer-aided-design (CAD) design software, then, the slicing software Cura Lulzbot® was used to generate gcode files for printing. In order to prevent any change in the properties of the material, the commercially available Chronosil pellets (Figure 17a) were dried in a vacuum oven (Lindberg/Blue M Vacuum Oven, Thermo Scientific) at 80 ℃ for at least 3 days to remove any possible moisture inside the pellets. After the pellets are dried, they were made into filaments (Figure 17b) a single-stage single-screw extruder (Filabot EX2, Triex LLC.) at 210 ℃ (Figure 17c).

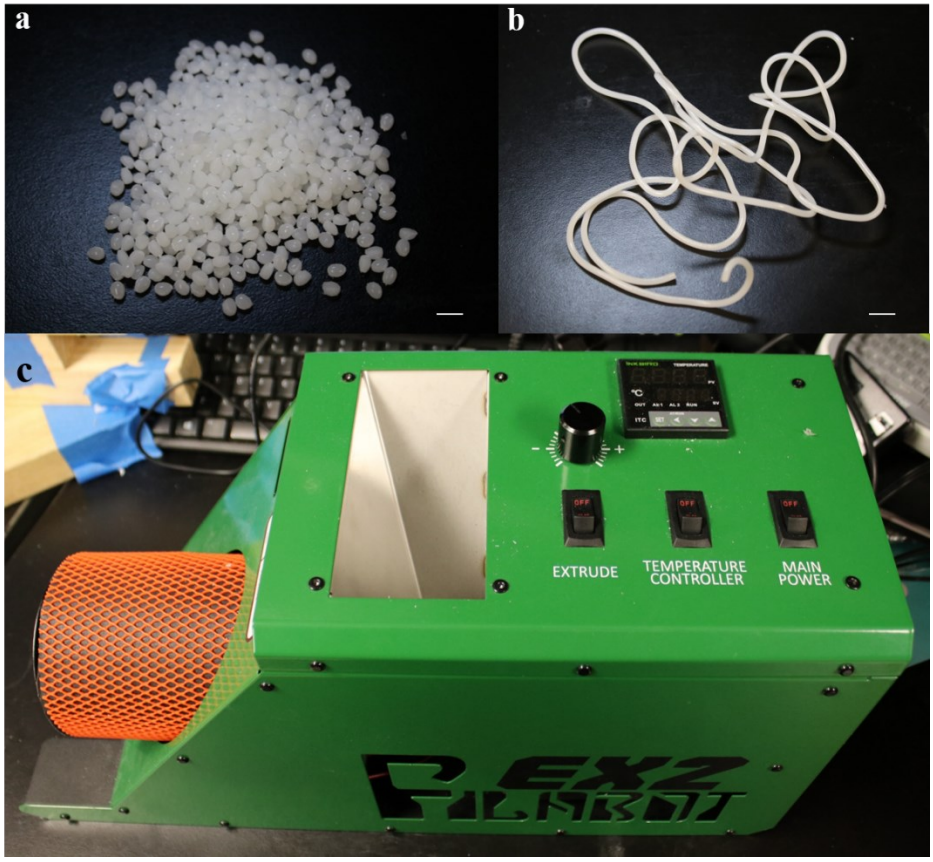

Figure 17: (a) Commercially available Chronosil pellets (scale bar is 1.5cm). (b) Filaments made from pellets ready for printing (scale bar is 1.5cm). (c) single-stage single-screw extruder to make filaments from pellets.

The structures were printed using Lulzbot TAZ 6 (Lulzbot) with a 0.35 mm nozzle head (LulzBot Flexystruder Tool Head v2, Lulzbot) at 260 ℃ (Figure 18), the printing speed was 9 mm/s, the layer thickness was 0.15 mm and the bed temperature was 50 ℃.

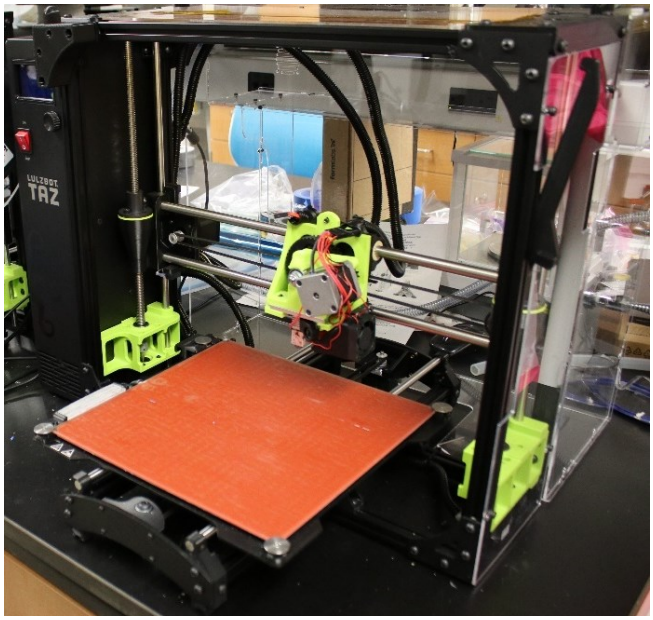

Figure 18: Photograph of Lulzbot TAZ 6 3D printer with LulzBot Flexystruder Tool Head v2.

2.4. Summary

In this chapter, we discussed the rationale of choosing thermoplastic polycarbonate-based polyurethane as our main 3D printing material and the thermal and rheological properties of chronosil were characterized. The resulting data were used as a guideline to process the material in FFF 3D printing.

Thermal and rheological properties are two important aspects in FFF process. Thermal measurements showed important thermal transition points and thermal stability of the chronosil. The first-order transition of chronosil was at around 160 ℃, and significant weight loss was observed at temperatures higher than 300 ℃. These results helped us determine the suitable printing parameters. Rheological properties showed the viscosity of chronosil was dependent on

the angular frequency and decreased as the angular frequency increased. The micro-CT scanning results further guided us choosing specific printing temperature, layer height and printing speed.

In the following chapter, we will discuss the design for RV-PA conduits and sutureless couplers respectively.

3. Design and 3D-printing cardiovascular devices

Our novel RV-PA conduits were designed to have folds that enabled the conduits to change shapes during the growth process, and the sutureless couplers were designed to have anchors on the two ends to enable sutureless vascular anastomosis. In the following sections, design details of shape-changing conduits and sutureless couplers will be described.

3.1. Shape-changing RV-PA conduits

Human body increases the body surface area progressively during growth especially during the growing from infant to young adult, and in order to provide enough nutrients and oxygen in the blood, the blood flow rates need to increase as well.[56] To accommodate the increase of blood flow rates, the systemic and pulmonary pressure levels will also increase in infants during growth (Figure 19a).[56] Here we focus specifically on the conduits used to treat defects in the pulmonary circulation caused by CHDs. The primary role of the right ventricle (RV) is to deliver all the blood it receives into the pulmonary circulation without causing right arterial pressure to rise,[57] if a conduit with a fixed size is used to treat CHDs in the pulmonary circulation, it eventually limits flow as the infant grows. With progressive mismatch in size and relative obstruction, RV pressure increases to abnormal levels. Hence, the ideal conduit should be designed to accommodate the changes in the blood flow and pressure levels during the growth by increasing its radial dimension as a function of age (Figure 19b). [58]

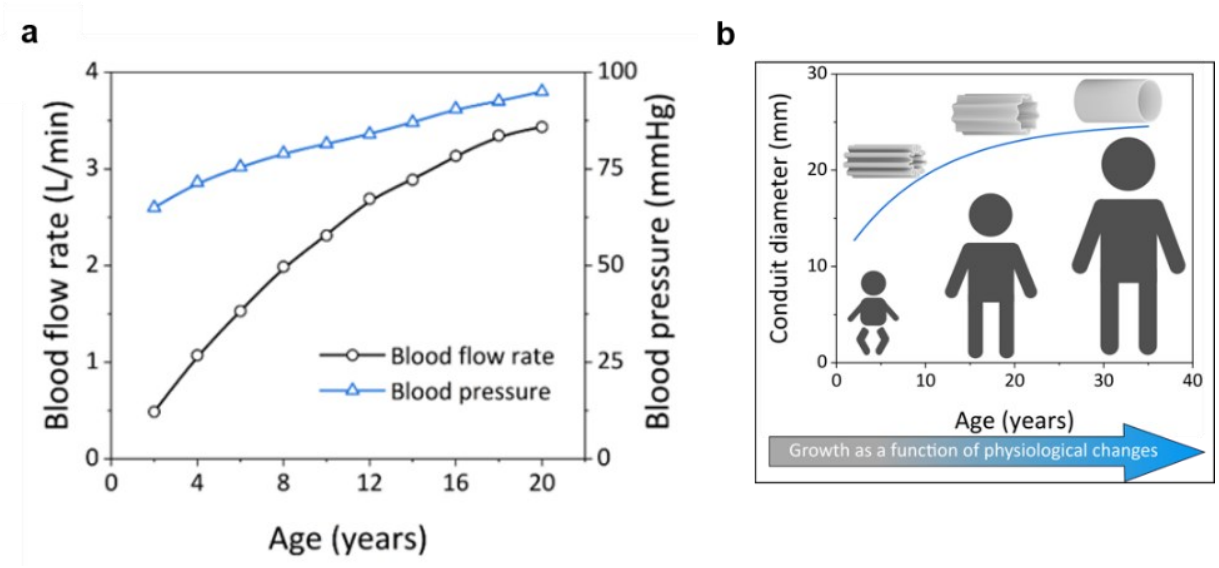

Figure 19: (a) Changes observed in the average blood flow rate and pressure levels in systemic circulation (b) Desired conduit effective diameter at different ages[xvi]

Inspired by the folded morphology in the human body such in the esophagus (Figure 20) in human body,[59] we designed folded patterns along the radial direction of the conduit to actualize the "growth" of the conduits (Figure 21a).

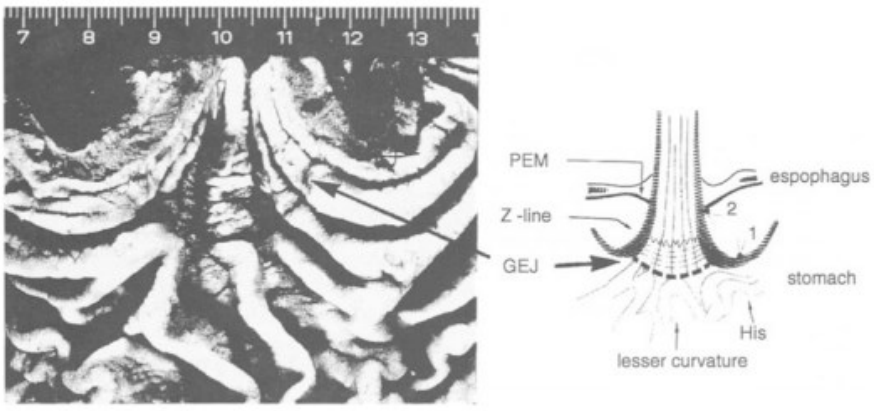

Figure 20: Specimen opened along the greater curve side shows the entire mucosal lumen of the esophagogastric junction.[xvii]

[xvi] Reprinted from Ozan Erol et al. 3D-Printed Shape-Changing Cardiovascular Conduits to Accommodate Growth of Pediatric Patients, in preparation.

[xvii] Reprinted by permission from Springer Nature Customer Service Centre GmbH: Springer Nature, Barrett's Esophagus, Anatomy and Embryology of the Esophagus, D. Liebermann — Meffert, Copyright (2001)

Fold geometries were designed such that all folds had the same radius of curvature to simplify the conduit design while the locations of folds were chosen as free design parameters. The conduits with radial folds can unfold as the blood flow rate and the pressure increase as a result of the growth of a pediatric patient (Figure 21b). The final diameters and unfolding behavior of the conduits can be adjusted by tuning the number of folds. The number of folds was kept even numbers to make the conduit cross sections always symmetric. The designed conduits were printed using Chronosil with the parameters described in section 2.2.3. layer by layer (Figure 21c) and further tested *in-vitro*.

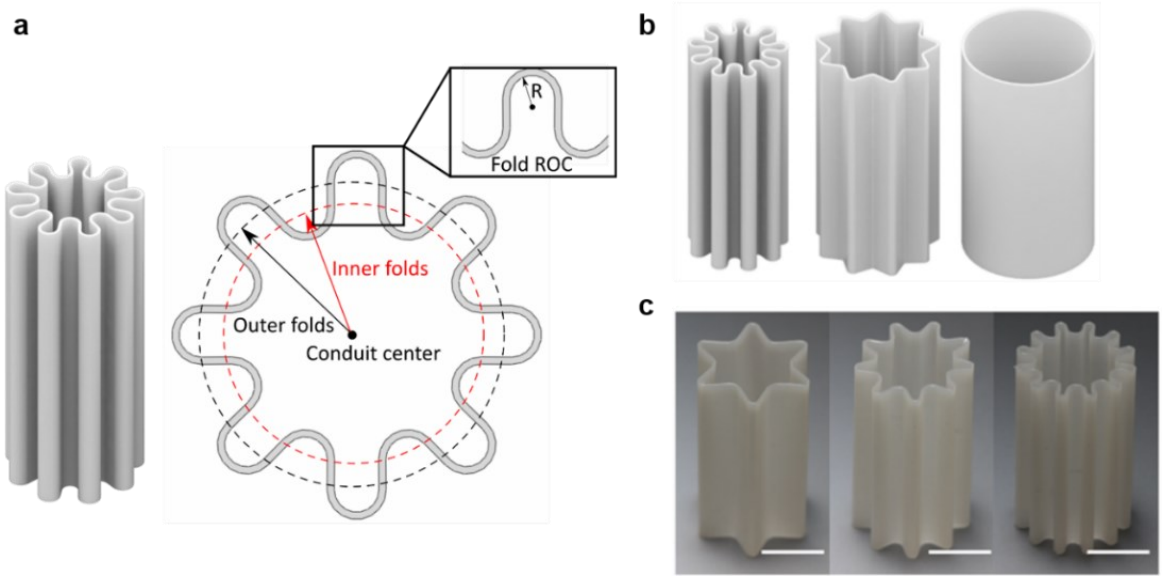

Figure 21: (a) Schematic showing the basic design concept of the conduits with radially distributed folds. (b) Schematic showing the progressive radial conduit expansion. (c) printed conduits with different number of folds (Scale bars are 10 mm).[xviii]

3.2. Sutureless coupler

Vascular and microvascular anastomosis is a technique used by surgeons and microsurgeons to connect two blood vessels end-to-end or side-to-end together with sutures. This must be done

[xviii] Reprinted from Ozan Erol et al. 3D-Printed Shape-Changing Cardiovascular Conduits to Accommodate Growth of Pediatric Patients, in preparation.

safely and quickly to limit ischemia time to downstream tissues and restore blood flow. In order to improve the efficacy of traditional suture method, we sought to design a one-piece biomedical device that can connect two blood vessels together without any suture or adhesives. Inspired by the wing-locking device in beetles,[60] we utilized a similar "hook" structure in our device, which we have termed "anchors". As shown in Figure 22, the curved anchors in the wings maximize lateral shear friction while minimizing vertical friction.

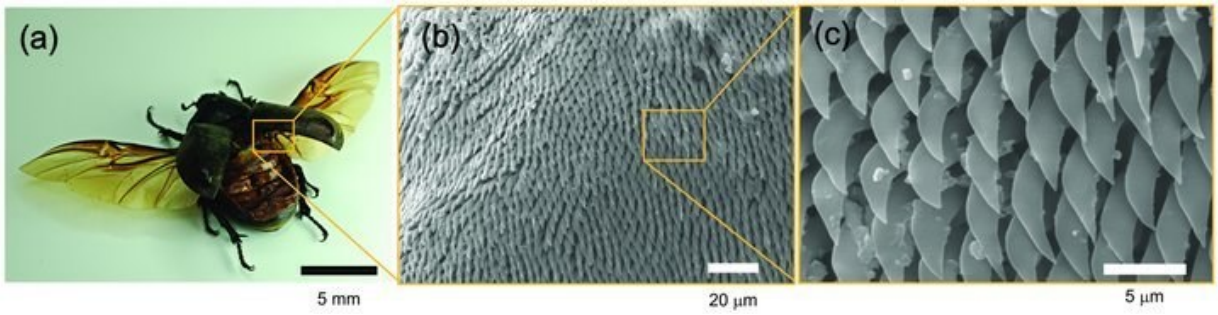

Figure 22: (a) Photograph of the wing-locking device of the beetle.(b,c) SEM images of microtrichia on the cuticular surface with two different magnifications.[xix]

The coupler was designed to have a flexible cylinder shape, and the peripheral surface of the two ends of the coupler are covered with unidirectional anchors (Figure 23a). When the coupler is inserted into a vessel, the direction of insertion is oriented to the direction of the anchors, which results in guarding (Figure 23b). If the coupler is pulled out in the opposite direction, the force will engage the anchors, thus disabling the coupler from being removed from the vessel. The couplers were designed to have 3 mm or 5 mm outer diameters to adapt different sizes of blood vessels, the ability to hold blood vessels together can be adjusted by varying the angles and numbers of the anchors.

[xix] Reprinted from Advanced materials, Pang et al., Bioinspired Reversible Interlocker Using Regularly Arrayed High Aspect-Ratio Polymer Fibers, Copyright © 2012 WILEY-VCH Verlag GmbH & Co. KGaA, Weinheim

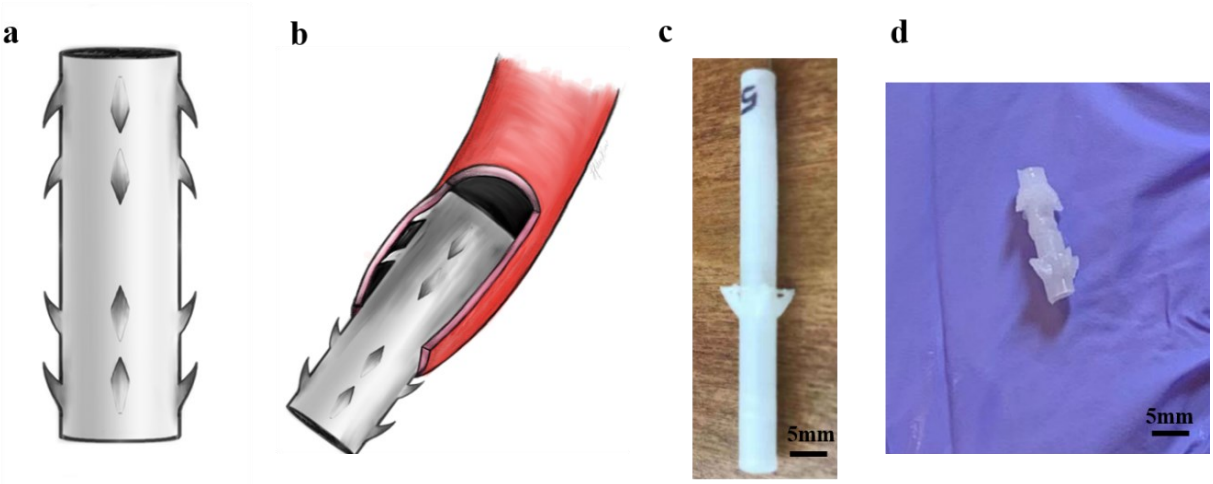

Figure 23: (a) Schematic illustration of designed sutureless coupler. (b) An illustration of coupler deployed in a blood vessel. (c) Printed sutureless coupler with anchors on one end and (d) two ends

The designed couplers were printed using Chronosil with the same parameters as the RV-PA conduits layer by layer without any supporting materials, so we were only able to print anchors on one end instead of two ends (Figure 23c). In order to get the fully printed device, we used glue to stick two prints together (Figure 23d).

3.3. Summary of design and 3D printing cardiovascular devices

The inspiration of designs for shape-changing RV-PA conduits and sutureless couplers are discussed in this chapter. Inspired by esophagus, the RV-PA conduits were designed to have folded structure that can expand as the blood flow rate increase, thus giving “growth” potential to 3D-printed conduits. The design of the sutureless couplers was inspired by the wing-locking device in beetles, the hooked anchors on two ends hold two blood vessels together without any sutures or adhesives.

In the following chapter, a bench-top circulatory loop will be described, and a couple of in-vitro tests of the shape-changing RV-PA conduits will be discussed.

4. *In-vitro* testing of RV-PA conduits

In order to demonstrate the changes of the conduits during growth, we developed an *in-vitro* bench-top circulatory loop to mimic the hemodynamic flow conditions. The designed experimental set up is based on a lumped parameter model, which simulates the blood circulation by introducing two building blocks in the electrical circuits.[61] One is a resistor, which represents resistance to flow in the circulation, the other one is capacitor, which represents the compliance of the system. These two blocks represent the whole body's total impedance. Resistance is defined as the pressure gradient per flow rate through the circulation, while compliance is defined as the change in blood volume due to a given change in blood pressure.

We did calibration to relate the experimental units in our setup to the physiological vascular resistances and compliances[62–64] before we did tests of RV-PA conduits. After calibration, several *in-vitro* tests were done to evaluate the performance of the conduits.

4.1. Overall *In-vitro* fluidics test setup

The bench-top circulatory loop consists of (1) adjustable compliance chambers, (2) variable flow resistances, (3) reservoir, (4) external conduit visualization setup (camera), (5) pressure sensors, and (6) digital flow meter. The loop was driven by a pulsatile positive displacement pump (Harvard Apparatus, Holliston, MA, USA) with adjustable stroke volume (SV) (15-100 mL), heart rate (0-100 beats per minute) (BPM) and output phase ratio (Figure 24).

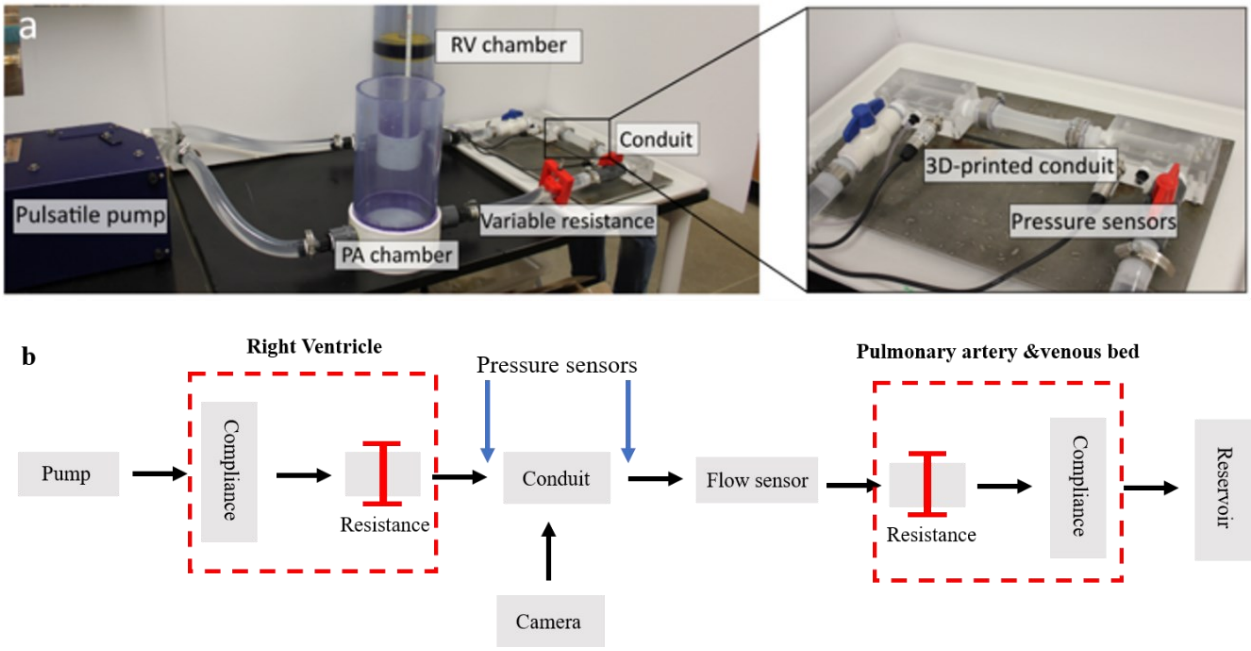

Figure 24: (a) In-vitro fluidics test setup capable of mimicking pediatric pulmonary circulation. [xx](b) Schematic of the components of the in-vitro fluidics test setup

The flow resistances were adjusted by custom made adjustable pinch clamps (Figure 25a). The compliance chambers were comprised of cylindrical columns with inlet and outlet ports, and an inflatable plug allowing the air to be trapped (Figure 26a). The external conduit visualization setup was used to capture the shape changes of the conduits with a digital camera (Canon EOS 80D, Canon Inc.). Pressure waveforms were recorded at the inlet and outlet locations of the conduits using pressure sensors (Omega Engineering, Norwalk, CT, USA). An ultrasonic flowmeter (Cynergy3, Wimborne, Unitied Kingdom) was used to measure the flow rate within the circulatory loop. Data from the pressure and flow sensors was collected with a dedicated 16-bit acquisition board NI USB-6210 (National Instruments Inc., Austin, RX, USA).

[xx] Reprinted from Ozan Erol et al. 3D-Printed Shape-Changing Cardiovascular Conduits to Accommodate Growth of Pediatric Patients, in preparation.

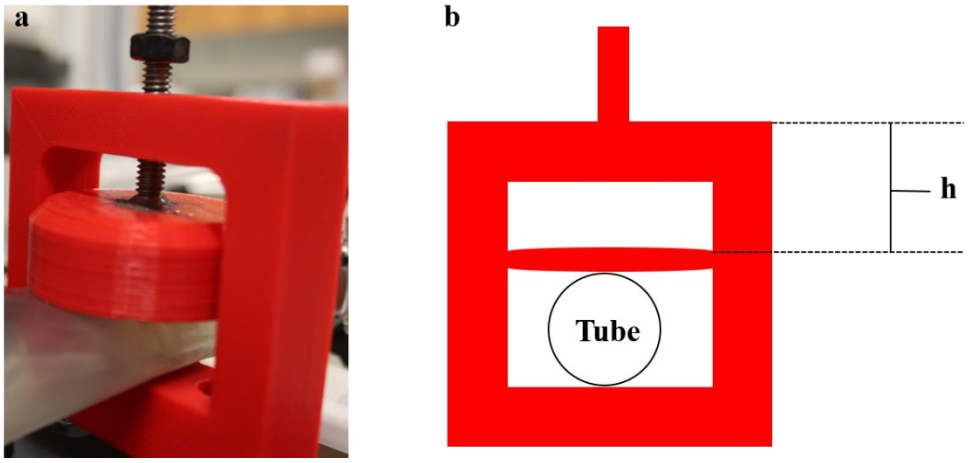

Figure 25: (a) The pinch clamp in the circulation system. (b) Schematic illustration of the pinch clamp and measurement of resistance distance

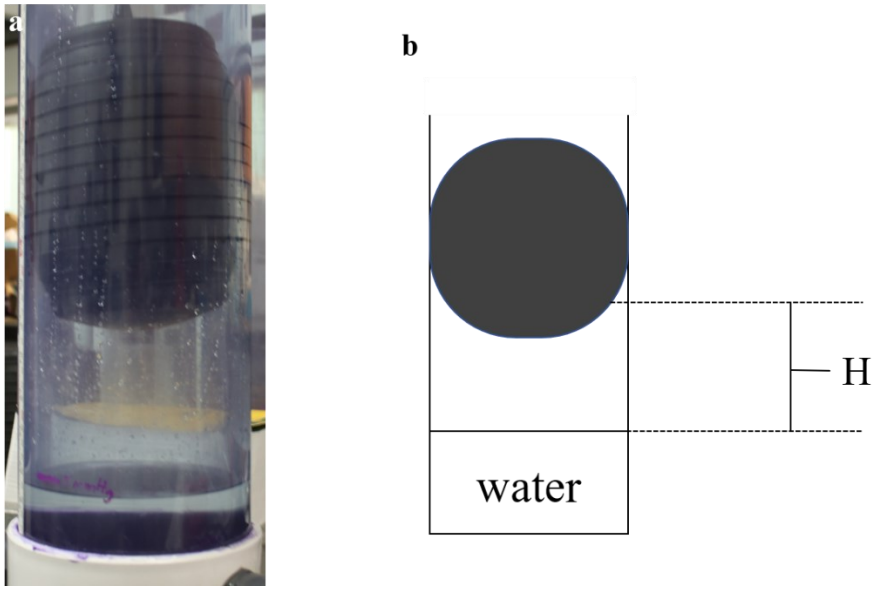

Figure 26: (a) The compliance chamber in the circulation system. (b) Schematic illustration of the compliance chamber and the height measurement, the height is defined as the distance between the third line from the bottom of the ball and the water before the ball is inflated.

In order to relate the physiological vascular resistances and compliances to the units in our developed circulatory loop, we calibrate the resistance units and compliance units separately. The flow rates used during the calibrations were 1.2, 2.4, 3.2 and 4.0 L/min. In all experiments, DI water was used as the fluid within the loop. The customized circulatory loop was used to mimic

the hemodynamic flow conditions at different ages for *in-vitro* tests of our printed conduits which will be discussed later.

4.1.1. Calibration of resistance units

The calibration of the flow resistances (pinch clamps) was conducted by measuring the pressure drop across the units at different pinch distances under different flow rates (Figure 27). The compliance level (H, as illustrated in Figure 26b) was 5 cm and the resistance distance (h, as illustrated in Figure 25b) varied between 28 mm and 32 mm with 1 mm increments.

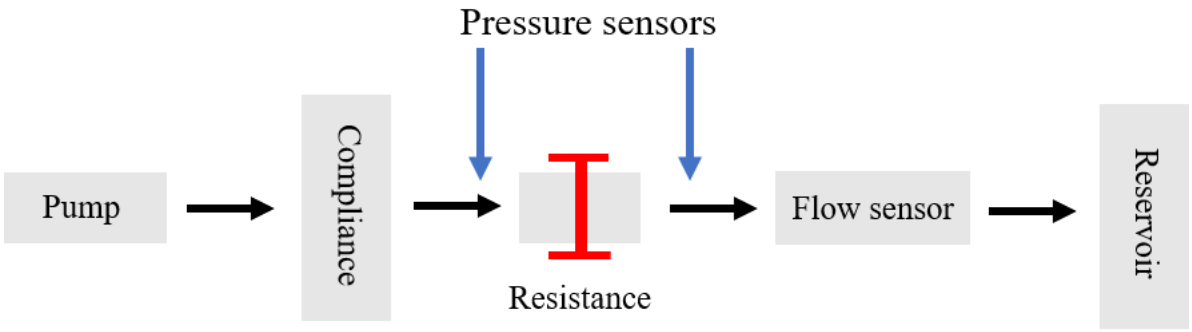

Figure 27: Schematic of the components of the resistance unit calibration setup.

The calibration curve (Figure 28) relating the pinch distance (D_R) to the flow resistance (F_R) was determined as ($R^2 = 0.97$):

$$\log(F_R) = 21.21 \log(D_R) - 31.37$$

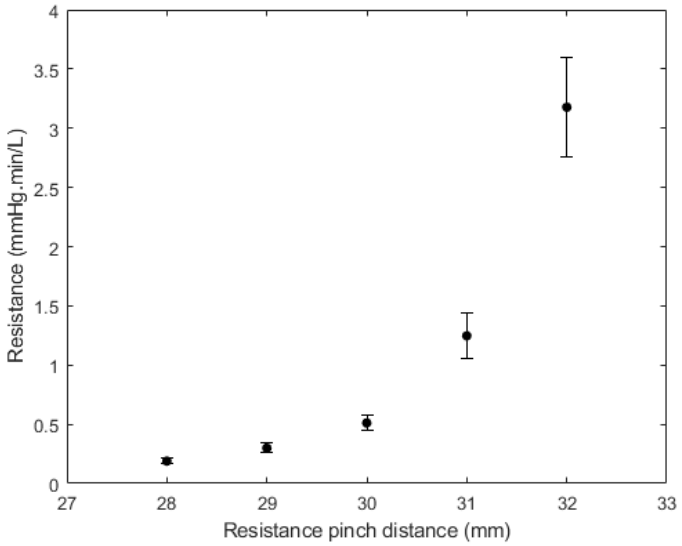

Figure 28: Calibration of the variable flow resistance in the developed in-vitro fluidics test setup (Error bars are average ± one standard deviation)

4.1.2. Calibration of the compliance units

The compliance chambers were also calibrated in a similar manner to the resistance unit where the amount of air trapped in the cylindrical columns were correlated by measuring the inlet and outlet pressures as well as the flow rate across the columns (Figure 29). The resistance distance was set to 30 mm. The air trapped varied between 5 cm and 15 cm with 2.5 cm increments, together with the minimum trapped air with was 3 cm.

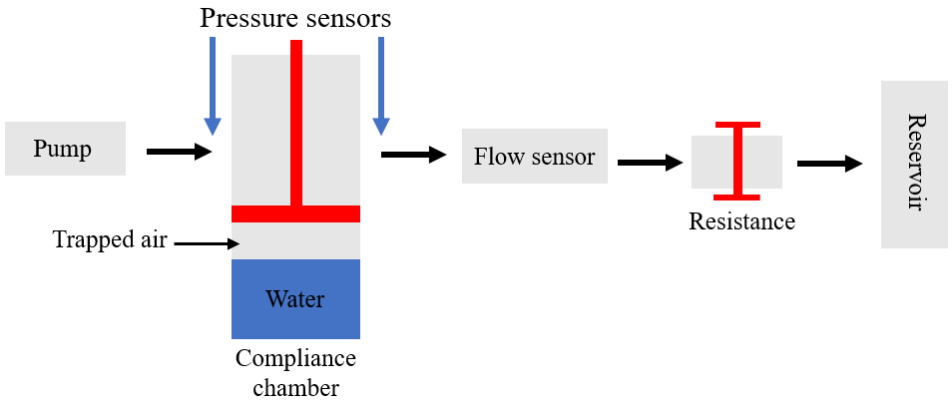

Figure 29: Schematic of the components of the resistance unit calibration setup

The calibration curve (Figure 30) relating the time-averaged compliance value (F_C) to the air trapped within the column (D_C) was obtained as ($R^2 = 0.93$):

$$F_C = 0.02345 D_C + 1.578$$

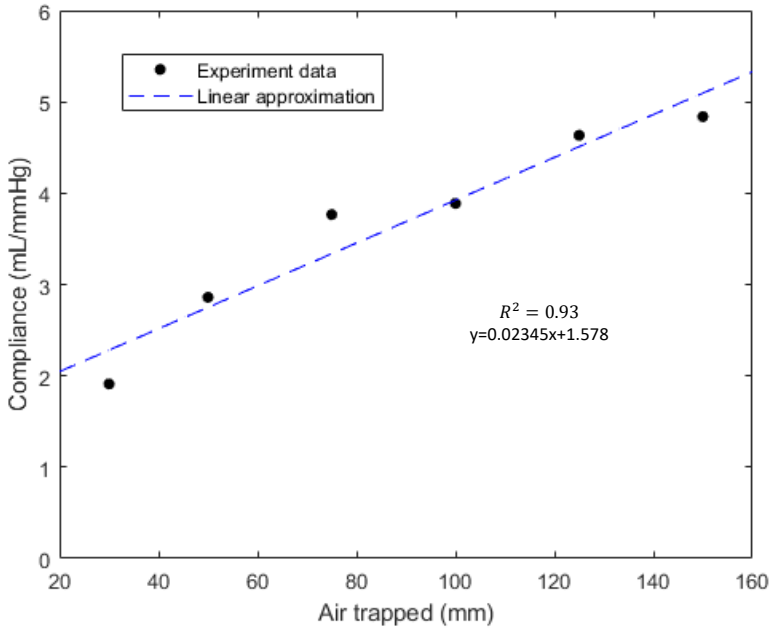

Figure 30: Time-averaged compliance values for the compliance chambers.

4.2. *In-vitro* characterization of 3D printed conduits

We used the customized *in-vitro* fluidics setup to study the burst pressure of the 3D printed conduits as well as their dynamic compliance and shape changing effect at different ages.

4.2.1. Burst pressure

The 3D-printed conduits should be able to reach the healthy adult blood pressure levels without bursting, hence, the burst pressure of the 3D-printed conduits was studied by injection of measured volumes of water to pressurize the conduits and measuring the pressure levels with the in-vitro fluidics setup (Figure 31).

The conduits were attached to the conduit compartment and filled with water until there were no bubbles within the conduits and attached tubes. The valves connecting the conduits from other parts in the setup were closed and the internal pressure of the conduits was equalized at the atmospheric pressure for further testing. After the pressure was equalized, the conduits were pressurized by injecting water in increments of 20 mL with a syringe.

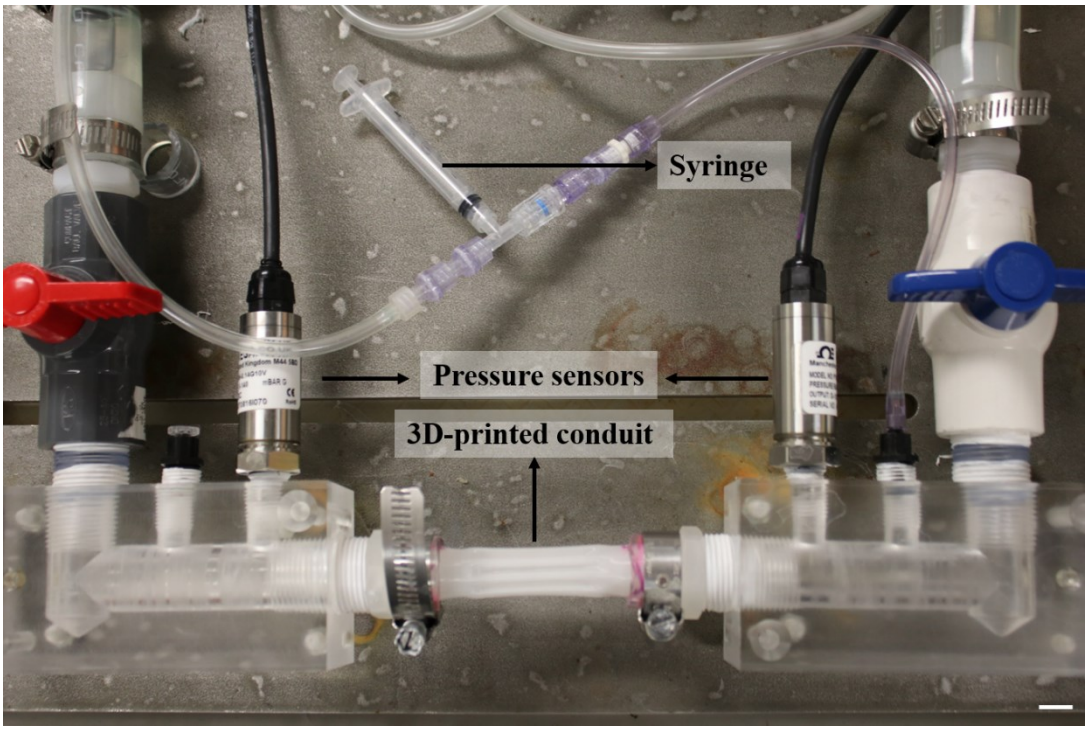

Figure 31: The burst pressure test set up (scale bar is 1cm).

The hydrostatic pressures within the conduits were recorded at 100 Hz by the pressure sensors. The 3D-printed conduits were able to withstand internal hydrostatic pressures of up to ~1000 mmHg without bursting which is much higher than the physiological pressure levels (<120 mmHg).

4.2.2. Dynamic compliance

Mismatch in the compliance properties of prosthetic graft and native artery have been a major cause of prosthetic graft failure because of distal anastomotic myointimal hyperplasia.[65,66] Hence, it is important that the conduits exhibit dynamic compliance as close as to the native tissues.

The dynamic compliances of the conduits were determined with in-vitro test setup at different dynamic pressure ranges. The total compliance of the fluidics setup was kept constant while the flow resistances were adjusted to achieve the targeted pressure levels during all the experiments. The compliance values were determined at pressure levels between 5-20 mmHg and 95-110 mmHg with 15 mmHg increments. The flow rate was also kept constant at 2.4 L/min (40 mL SV and 60 BPM). The change in the effective diameters of the conduits were recorded with a camera and processed with code written in MATLAB R2017B later.

We 3D printed conduits with 12, 16 and 20 folds to determine the effect of the number of folds while the radius of curvature (ROC) was kept constant at 2mm (Figure 32a). In addition, two different conduit designs were 3D-printed with 2 mm and 3 mm ROCs to study the ROC effect. Both conduits had 16 folds (Figure 32 b and c).

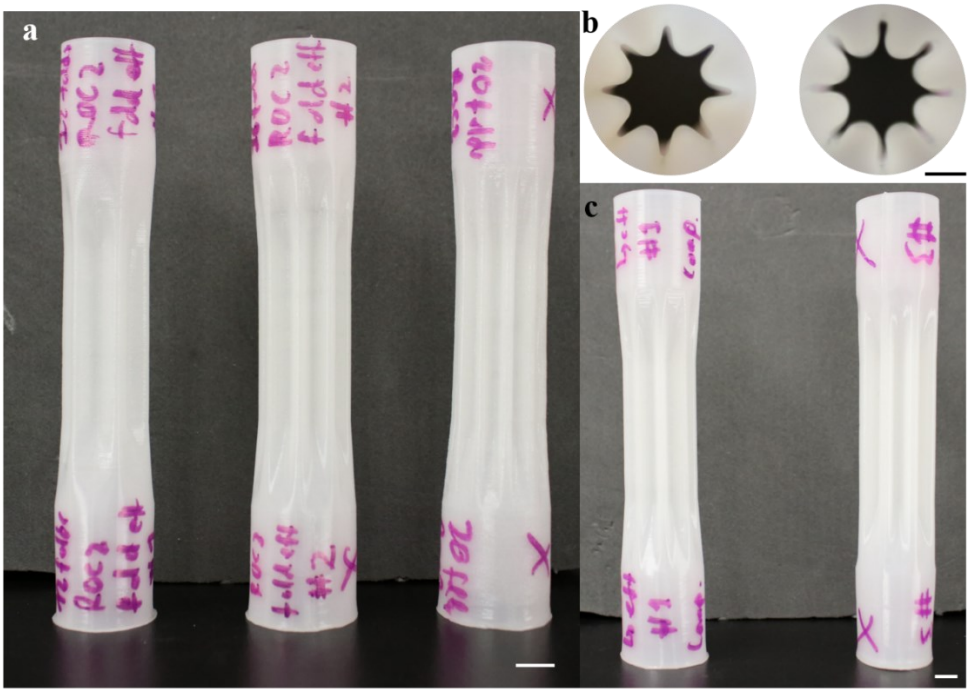

Figure 32: Photographs of 3D-printed conduits having (a) different numbers of folds. left: 12 folds, middle: 16 folds, right: 20 folds. Scale bar is 5mm. (b) different radius of curvature from upside view. Left: 2mm, right: 3mm. Scale bar is 3mm. (c) different radius of curvature. Left: 2mm, right: 3mm. Scale bar is 5mm.

The percent dynamic compliances (C) per 15 mmHg were determined using the following equation:[66]

$$\%\mathrm{C} = 100\frac{{}^{D_s - D_d}/_{D_d}}{P_s - P_d}$$

where D_s and D_d are systolic and diastolic diameter, and P_s and P_d are systolic and diastolic pressure respectively.

Figure 33a shows the effect of the number of folds on the dynamic compliance of the conduits. Figure 33b shows the effect of ROC on the dynamic compliance of the conduits. We observed that the increased number of folds resulted in higher dynamic compliances. We also observed that the dynamic compliance values were reduced as the pressure levels increased, similar changes were also observed when radius of curvature of the conduits was increased. This was mainly due to the expansion of conduits and reaching their targeted final diameters as the pressure increased.

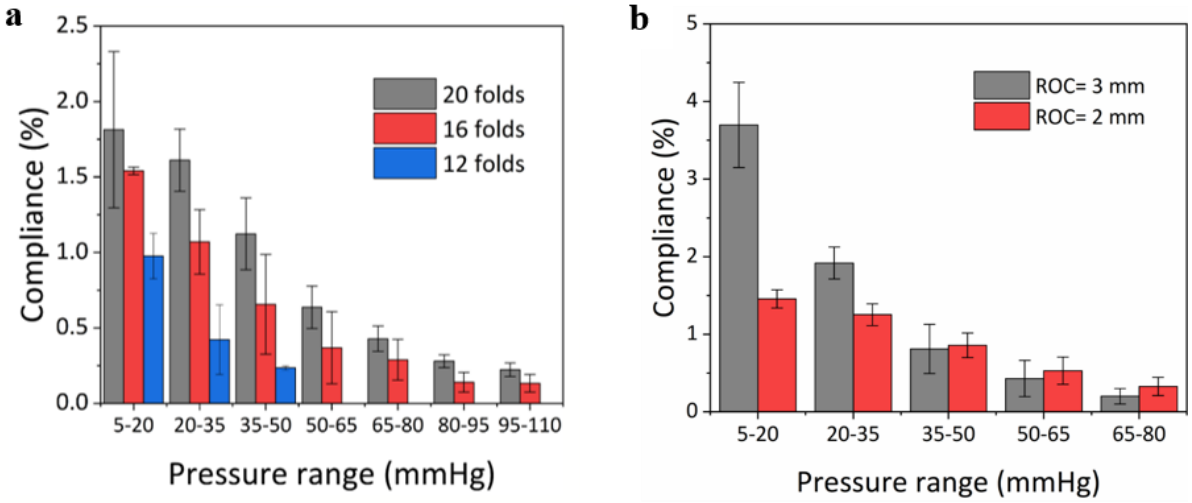

Figure 33: Dynamic compliance values of 3D-printed conduits with (a) different numbers of folds, (b) different radius of curvature[xxi]

[xxi] Reprinted from Ozan Erol et al. 3D-Printed Shape-Changing Cardiovascular Conduits to Accommodate Growth of Pediatric Patients, in preparation.

4.2.3. Functionality tests

As mentioned in section 3.1, the RV-PA conduit should be able to expand in order to compensate higher blood flow during growth, if the conduit is fixed in size, it becomes a fixed resistor and the systolic pressure will increase as the blood flow rate increases.[67] Thus, our shape changing conduit should maintain lower systolic pressures as flow rates rise, as compared with the conduits with fixed diameter.

In order to test the growth potential of the 3D-printed conduits, the compliance chambers and variable resistance units were set to have a certain impedance values (defined as multiplication of resistance and set compliance values). Table 1 shows the potential compliance and resistance values considered during the functionality experiments with 5 mL/mmHg compliance and 0.8 mmHg-min/mL resistance, corresponding to healthy six-year-old impedance value.[62,64] The conduits were tested at different impedance values in Table 1 by varying resistance units and compliance chambers based on the calibration curves developed in 4.1.

Impedance (min × 10^{-3})		**Compliance (mL/mmHg)**		
		2.5	5	10
Resistance (mmHg.min/L)	0.4	1	2	4
	0.8	2	4	8
	1.6	4	8	16

Table 1: Compliance and resistance values considered for the functionality experiments (Red box indicates the values used for 6-year-old conditions)[xxii]

[xxii] Reprinted from Ozan Erol et al. 3D-Printed Shape-Changing Cardiovascular Conduits to Accommodate Growth of Pediatric Patients, in preparation.

We mimicked the hemodynamic conditions determined from clinical data for ages of 6, 10, 14, 18 and 22[56,68,69] using our fluidic setup (Table 2). The stroke volume and beats per minute were changed while the impedance of the system was kept constant.

	Age (years old)				
	6	10	14	18	22
Heart rate (bpm)	94	83	77	71	70
Stroke volume (mL)	16	28	38	47	50

Table 2: Hemodynamic conditions at different ages employed for functionality experiments of the shape-changing conduits

The flow rate and the inlet and outlet pressure waveforms were recorded during the experiments through sensors at 100 Hz while the cardiac output was monitored with the ultrasonic flowmeter. A digital camera was used to record the changes in the effective diameter of the conduits as the hemodynamic conditions changed at the rate of 25 frames per second (fps). The system was run for three minutes to ensure steady-state conditions for each age condition and the data was collected over 1 minute. A custom image processing code was used to extract the effective diameter values and the collected data was time-averaged to correlate the age-based hemodynamic conditions to the shape-changing functionality of the 3D-printed conduits. In order to compare the pressure gradients across conduits between the shape-changing conduits and conduits with a fixed diameter, we tested 10 mm diameter conduits with different number of folds (12, 16 and 20), together with a 3D-printed conduit with a fixed 16 mm diameter with the same hemodynamic conditions (Figure 34).

Figure 34: Photograph of (a) 3D-printed conduit of fixed 16 mm diameter (b) 3D printed conduit having 16 folds, radius of curvature is 2mm. (scale bar is 5 mm)

We observed that the effective diameters of the conduits increase as the flow rates increased in a pattern expected for a growing child (Figure 35a), the conduits can expand and reach up to about 17.5 mm of effective diameter (Figure 35b) at flow rates anticipated at the age of 20 years. The systolic pressure measured for the control conduits were higher compared to shape-changing conduits for the ages of 12, 16 and 20 as the blood rate increased (Figure 35c).

Figure 35: (a) Radial expansion of the conduit with 16 folds (Scale bar is 10 mm). (b) *In-vitro* effective conduit diameter change as a function of age. (c) Systolic pressure difference between the baseline conduit and shape changing conduits where baseline conduits had higher systolic pressure levels.[xxiii]

4.3. Summary

In this chapter, a customized bench-top circulatory loop system was described. The circulation system has two main adjustable units which can adjust the resistance and compliance in the system. We did calibration tests to relate the resistors and capacitors to the flow resistance and system compliance respectively.

The burst pressure test was done and the 3D-printed conduits showed the capacity to reach much higher blood pressure level (1000 mmHg) than the healthy adult blood pressure levels (120 mmHg) without bursting. The dynamic compliance of the 3D-printed conduits was also characterized, different pressure ranges (5-20 mmHg and 95-110 mmHg with 15 mmHg increments) were selected and compliance at every pressure range was calculated. We varied the number of folds of the conduits while the radius of curvature (ROV) was fixed at 2 mm, the dynamic compliance of the conduits increases as the number of folds increases. We also varied the ROC while the number of the folds was fixed at 16, similar changes in compliance was observed,

[xxiii] Reprinted from Ozan Erol et al. 3D-Printed Shape-Changing Cardiovascular Conduits to Accommodate Growth of Pediatric Patients, in preparation.

showing that the compliance can be tuned by adjusting the geometric parameters. Finally, we adjusted the stroke volume (SV, mL) and beats per minute (BPM) to mimic the hemodynamic conditions at age 6, 10, 14, 18 and 22. The SV was set to 16, 28, 38, 47, 50 and the BPM was set to 94, 83, 77, 71, 70, respectively. The effective diameters of the conduits were recorded using a camera and we observed that the effective diameter increases as the age increases, the effective diameter of conduits can reach up to 17.5mm at age of 20, while the original diameter of the conduits is 10mm. Pressure waveforms at the inlet and outlet locations of the conduits were recorded with pressure sensors while the cardiac output was monitored with an ultrasonic flowmeter. The systolic pressure difference between the shape-changing conduits and the fixed size conduits were obtained. In the next chapter, several *ex-vivo* tests of the 3D-printed sutureless couplers will be described.

5. *Ex-vivo* testing of sutureless couplers

The two most important functions of the 3D-printed sutureless couplers are the simplicity to deploy and the ability to restore blood flow after the device is deployed. In this chapter, the feasibility of our 3D-printed sutureless couplers will be described, as well as the preliminary test results of leakage under different volumes of flow.

5.1. Feasibility

The 3D-printed sutureless coupler (Figure 22d) was deployed into ligated porcine carotid artery segments within 30 seconds, which is significantly faster than 2 hours when using traditional method. As shown in Figure 36a, the two separate blood vessels were fixed on a foam covered by surgical cloth using pins. Tweezers were used to insert the coupler into the ends of blood vessels. After the two blood vessels were connected, the anchors can remain in the intima of the blood vessels when it is stretched (Figure 36b) at forces beyond physiologic forces normally faced by anastomosed blood vessels. These tests show the feasibility of 3D-printed one-piece sutureless couplers.

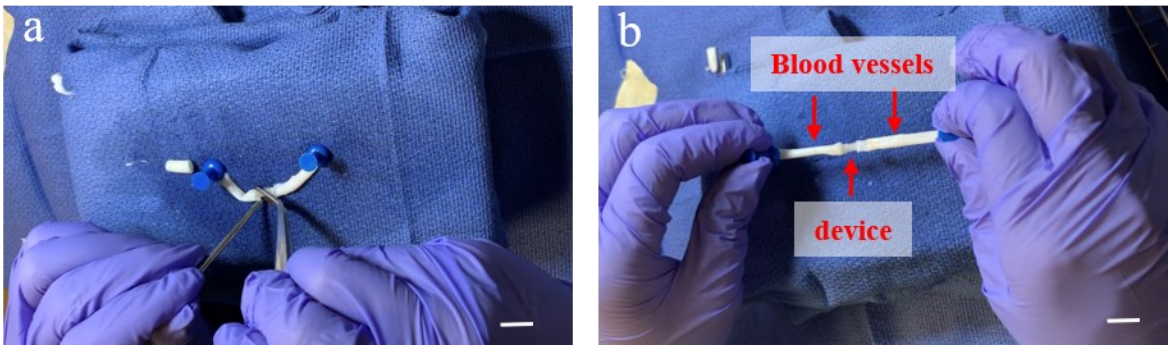

Figure 36: (a) Process of inserting 3D-printed coupler into blood vessels. (b) Stretching the connected blood vessels. (Scale bars are 3cm)

5.2. Flow tests

In order to test the ability of our device to restore blood flow after connecting two blood vessels together, we used similar settings as Elliott *et al.* used in their study of immediate perfusion of small-diameter vascular grafts (sdVGs)[70]. As shown in Figure 37 a and b, the connected blood vessels using 3D-printed sutureless coupler was encased in a single-chamber bioreactor. Phosphate-buffered saline (PBS) which is a buffer solution commonly used in biological research was used as the liquid in the system. Red dye was added to visualize the leakage in the bioreactor, and can be quantified via Ultraviolet–visible spectroscopy. Several safety stiches were set at the connections between needles and blood vessels. A safety stich was also set at the connection between two blood vessels.

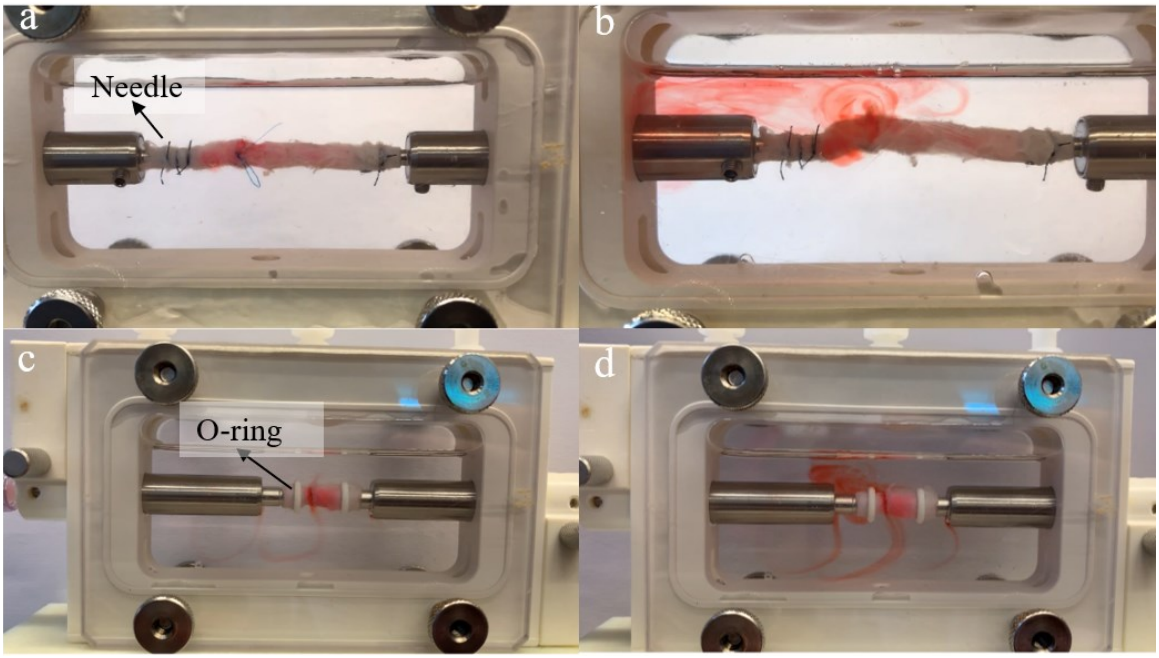

Figure 37: Sutureless coupler connected blood vessels under flow rates at (a) 30 mL/min (b) 40 mL/min. Traditional sutured blood vessels under flow rates at (c) 60 mL/min (d) 160 mL/min.

In order to compare the ability of the blood vessels connected with sutureless couplers to endure flow to that of traditional sutured blood vessels, we did the same tests with sutured ones. The blood flow rate in arteries with diameters ranging from 0.8 mm to 1.8mm is 3.0-26 ml/min.[71]

As shown in Figure 37 c and d, O rings were used to secure the connections of the needle and blood vessels. The sutureless coupler experienced significantly leakage from a branch artery that was still patent from the carotid artery when the flow rate went to 40 mL/min, which is a much higher than a physiological condition, while the traditional sutured ones was able to endure flow rate until 160 mL/min when the leakage started. Although we were not able to reach the highest flow rate that the sutureless coupler connected site can sustain because of leakage from other sites, it is still promising that our 3D-printed sutureless couplers can work and stay in place at certain blood flow rate.

5.3. Summary

In this chapter, we discussed the feasibility and the ability to restore blood flow using our 3D-printed sutureless couplers. Preliminary data shows that the sutureless coupler can be deployed more rapidly than traditional suture methods which take around two hours to finish. In addition, the blood vessels connected with sutureless couplers can restore blood flow with flow rate up to 40 mL/min which is higher than normal arterial blood flow rate. However, there is still much work that can be done to better understand the behavior of connected blood vessels using sutureless coupler, and this will be discussed in the following chapter.

6. Conclusion and future directions

The two main sections of this thesis are as follows: 1) Design and testing of RV-PA conduits; and 2) Design and preliminary test of sutureless couplers.

6.1. RV-PA conduits

6.1.1. Conclusion

We utilized bioinspired folding morphologies to design novel RV-PA conduits for the treatment of CHDs, the conduits were fabricated using 3D printing with a biostable, biocompatible and soft elastomers. The printing parameters was decided as 260 ℃ printing temperature, 0.15mm layer height and 9mm/s speed based on the study done by Bachtiar et al.[53].

The shape-changing conduit design that we tested has radial folds. The folds are opened by blood pressure increment in growing pediatric patients. As the radial folds open, the luminal cross section increases in size, reducing flow resistance. We studied the capability of the printed conduits to hold pressures. The 3D-printed conduits were able to withstand high pressures up to 1000 mmHg without bursting. The dynamic compliance in the pulmonary circulation system was studied with different conduits. The conduits showed the ability to adjust the compliance by tuning number of folds and radius of curvature of the conduits. We also observed that the dynamic compliance values were reduced as the pressure levels increased, this is due to the expansion of the conduits and reaching the final diameters as the pressure level increases. Then we demonstrated the growth potential of the conduits under different hemodynamic conditions, corresponding to those of different ages. The shape-changing conduits showed superior performance compared to fixed size conduits as there was a decrease of up to 5 mmHg in systolic pressure when the conduits had 20 folds. The effective diameter of conduits can reach up to 17.5mm at age of 20, while the original effective diameter is 10mm.

More work can be done as a follow-up on this study, the following section will discuss about future work.

6.1.2. Future directions

As our 3D-printed conduits are for applications as a cardiovascular implant, fatigue life is a very important property as the human heart beats a hundred thousand times a day. Conducting a fatigue test and mimicking the physiological environment, e.g. immersing in PBS at 37 ℃ will be very beneficial. Besides the fatigue tests, surface modification of the conduits can be another topic to study. Although Chronosil has been proved to be biocompatible[53], blood coagulation and thrombosis resulting from blood–material interactions remain a challenge. Possibility of absorption of protein by the material will cause platelet adhesion and thrombus formation on surfaces.[72] Hence, it is important to control the surface properties including surface chemistry, and surface topology after we 3D-printed conduits. For example, strategies to create slippery liquid-infused porous surfaces (SLIPS) that can repel liquids have been developed recently.[73] It repels blood better than usual hydrophobic Teflon surfaces (Figure 38). Utilizing SLIPS strategy, the surface property of the 3D-printed conduits can be improved and decrease the possibility of thrombosis after implantation.

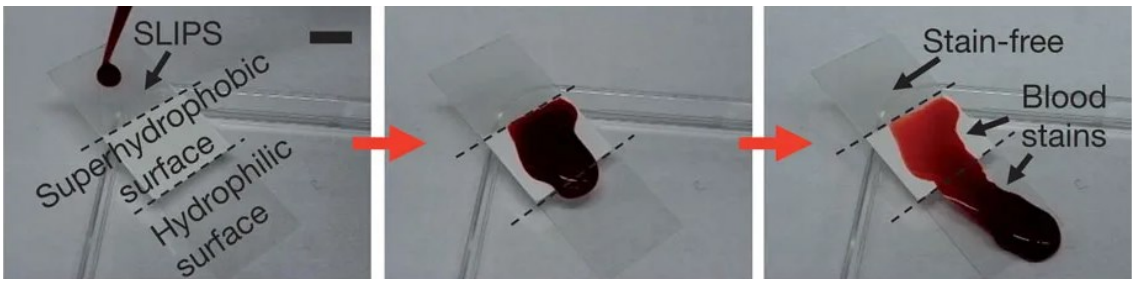

Figure 38: Comparison of the ability to repel blood by a SLIPS, a superhydrophobic Teflon porous membrane, and a flat hydrophilic glass surface.[xxiv]

[xxiv] Reprinted by permission from Springer Nature Customer Service Centre GmbH: Springer Nature, Nature, Bioinspired self-repairing slippery surfaces with pressure-stable omniphobicity, Tak-Sing Wong et al. Copyright (2011)

During the in-vitro tests, we only mimicked the hemodynamic conditions at age 6, 10, 14, 18 and 22, however, the flow rate changes rapidly during young age state, and we did not have the clinical data of the children with CHDs. More clinical data is needed to mimic the hemodynamic conditions especially from age 1 to age 10. In addition, we can further improve the *in-vitro* testing by using blood instead of water. As discussed before, thrombosis is one possible problem that can cause failure of the device. More *in-vitro* tests need to be done after surface treatment, e.g. SLIPS.

In addition, we have not yet done *ex-vivo* or *in-vivo* experiments to test the behavior of the conduits in animals, and applicability of the 3D-printed conduits for patients is still not clear. Further study to employ the 3D-printed conduits into animal models with long-time monitoring is necessary.

6.2. Sutureless couplers

6.2.1. Conclusion

Besides the RV-PA conduits, we were able to prototype the sutureless couplers that can significantly help vascular and microvascular anastomosis surgeries by shortening the learning curve and surgery time, and decrease the possibility of failure and complications. Preliminary data have shown the feasibility of replacing traditional suture method with our sutureless couplers, which can be deployed faster and easier. In addition, the capability of sutureless couplers to restore blood flow was evaluated. The evaluation results showed the couplers could endure flow rate up to 40 mL/min which is higher than regular blood flow rate in small diameter (0.8-1.0 mm) arteries. However, there is still much work to do which will be discussed in the following section.

6.2.2. Future directions

As discussed in section 3.2, we used FFF 3D printing technology to print the sutureless couplers, the resolution of the printing process is not high enough (0.15 mm layer height), which

is not very ideal for our final goal to prototype sutureless couplers for microvascular anastomosis. Also, we didn't use any supporting material to support the over-hanging anchors and we had to use glue to stick two separate half-couplers together to fabricate the final structure. Other possibilities of additive manufacturing method should be discovered. For example, we can use stereolithography, which generally has a higher resolution (for example 50 μm layer height and 25 μm x-y axis resolution in the case of Formlab 3B) to prototype our sutureless couplers. It also enables supporting structures using the same material that can be removed after post processing, which provides us capability to print the whole couplers in one print. However, the material choices are limited, where we cannot use chronosil as printing material in stereolithography, more additive manufacturing methods need to be explored. Blood vessels can grow and heal after around 6 months, biodegradable materials should be considered as the device can be removed after the blood vessels are healed.

The leakage tests were very simple and they were not conducted using a "one-piece" sutureless coupler, more leakage tests should be done using "one-piece" couplers. The geometric parameters including the angle of the anchors and the number of the anchors need to be further studied to finalize the design. In addition, the strength of the sutureless coupler when holding two blood vessels together need to be quantified using tensile testing machine.

The bench-top circulatory loop that we customized for *in-vitro* tests of RV-PA conduits can be developed to mimic human physiological situation, and utilized to evaluate the performance of sutureless couplers connecting blood vessels, including the burst pressure, the pressure gradient and be compared with traditional sutured blood vessels. *In-vivo* tests including deploying sutureless couplers into large animal models need to be done and this will require survival surgery and postoperative observation.

Bibliography

(1) Zadpoor, A. A. Design for Additive Bio-Manufacturing: From Patient-Specific Medical Devices to Rationally Designed Meta-Biomaterials. *Int. J. Mol. Sci.* **2017**, *18* (8).

(2) Standard Terminology for Additive Manufacturing – General Principles – Terminology. 15AD.

(3) Wong, K. V.; Hernandez, A. A Review of Additive Manufacturing. *ISRN Mech. Eng.* **2012**, *2012*, 1–10.

(4) Ligon, S. C.; Liska, R.; Stampfl, J.; Gurr, M.; Mülhaupt, R. Polymers for 3D Printing and Customized Additive Manufacturing. *Chem. Rev.* **2017**, *117* (15), 10212–10290.

(5) Ma, Y.; Hu, N.; Liu, J.; Zhai, X.; Wu, M.; Hu, C.; Li, L.; Lai, Y.; Pan, H.; Lu, W. W.; et al. Three-Dimensional Printing of Biodegradable Piperazine-Based Polyurethane-Urea Scaffolds with Enhanced Osteogenesis for Bone Regeneration. *ACS Appl. Mater. Interfaces* **2019**, *11* (9), 9415–9424.

(6) Norman, J.; Madurawe, R. D.; Moore, C. M. V.; Khan, M. A.; Khairuzzaman, A. A New Chapter in Pharmaceutical Manufacturing: 3D-Printed Drug Products. *Adv. Drug Deliv. Rev.* **2017**, *108*, 39–50.

(7) Ahangar, P.; Cooke, M. E.; Weber, M. H.; Rosenzweig, D. H. Current Biomedical Applications of 3D Printing and Additive Manufacturing. *Appl. Sci.* **2019**, *9* (8).

(8) Vignesh, U.; Mehrotra, D.; Dichen; Anand, V.; Howlader, D. Three Dimensional Reconstruction of Late Post Traumatic Orbital Wall Defects by Customized Implants Using CAD-CAM, 3D Stereolithographic Models: A Case Report. *J. Oral Biol. Craniofacial Res.* **2017**, *7* (3), 212–218.

(9) Hollister, S. J. Paediatric Devices That Grow Up. *Nat. Biomed. Eng.* **2017**, *1* (10), 777–778.

(10) Morrison, R. J.; Hollister, S. J.; Niedner, M. F.; Mahani, M. G.; Park, A. H.; Mehta, D. K.; Ohye, R. G.; Green, G. E. Mitigation of Tracheobronchomalacia with 3D-Printed Personalized Medical Devices in Pediatric Patients (Science Translational Medicine (2015) 7 (287er4)). *Sci. Transl. Med.* **2015**, *7* (287), 1–12.

(11) Feins, E. N.; Lee, Y.; O'Cearbhaill, E. D.; Vasilyev, N. V.; Shimada, S.; Friehs, I.; Perrin, D.; Hammer, P. E.; Yamauchi, H.; Marx, G.; et al. A Growth-Accommodating Implant for Paediatric Applications. *Nat. Biomed. Eng.* **2017**, *1* (10), 818–825.

(12) Zarek, M.; Mansour, N.; Shapira, S.; Cohn, D. 4D Printing of Shape Memory-Based Personalized Endoluminal Medical Devices. *Macromol. Rapid Commun.* **2017**, *38* (2), 1–6.

(13) Petrini, J.; Damus, K.; Russell, R.; Poschman, K.; Davidoff, M. J.; Mattison, D. Contribution of Birth Defects to Infant Mortality in the United States. *Teratology* **2002**, *66* (SUPPL. 1).

(14) Kevin Range, and D. M. Y. A. M. Confocal Imaging-Guided Laser Ablation of Basal Cell Carcinomas: An Ex Vivo Study. *Bone* **2012**, *23* (1), 1–7.

(15) Fahed, A. C.; Gelb, B. D.; Seidman, J. G.; Seidman, C. E. Genetics of Congenital Heart Disease: The Glass Half Empty. *Circ. Res.* **2013**, *112* (4), 707–720.

(16) Townsley, M. M.; Windsor, J.; Briston, D.; Alegria, J.; Ramakrishna, H. Tetralogy of Fallot: Perioperative Management and Analysis of Outcomes. *J. Cardiothorac. Vasc. Anesth.* **2019**, *33* (2), 556–565.

(17) Alsoufi, B. Right Ventricle-to-Pulmonary Artery Conduits: Do We Really Have an Option? *J. Thorac. Cardiovasc. Surg.* **2016**, *151* (2), 442–443.

(18) Salem, A. M. Right Ventricle to Pulmonary Artery Connection: Evolution and Current Alternatives. *J. Egypt. Soc. Cardio-Thoracic Surg.* **2016**, *24* (1), 47–57.

(19) Caldarone, C. A.; McCrindle, B. W.; Van Arsdell, G. S.; Coles, J. G.; Webb, G.; Freedom, R. M.; Williams, W. G. Independent Factors Associated with Longevity of Prosthetic Pulmonary Valves and Valved Conduits. *J. Thorac. Cardiovasc. Surg.* **2000**, *120* (6), 1022–1031.

(20) Poynter, J. A.; Eghtesady, P.; McCrindle, B. W.; Walters, H. L.; Kirshbom, P. M.; Blackstone, E. H.; Husain, S. A.; Overman, D. M.; Austin, E. H.; Karamlou, T.; et al. Association of Pulmonary Conduit Type and Size with Durability in Infants and Young Children. *Ann. Thorac. Surg.* **2013**, *96* (5), 1695–1702.

(21) Mery, C. M.; Guzmán-Pruneda, F. A.; De León, L. E.; Zhang, W.; Terwelp, M. D.; Bocchini, C. E.; Adachi, I.; Heinle, J. S.; McKenzie, E. D.; Fraser, C. D. Risk Factors for Development of Endocarditis and Reintervention in Patients Undergoing Right Ventricle to Pulmonary Artery Valved Conduit Placement Read at the 95th Annual Meeting of the American Association for Thoracic Surgery, Seattle, Washington, Apri. *J. Thorac. Cardiovasc. Surg.* **2016**, *151* (2), 432-441.e2.

(22) Breuer, C. K.; Brennan, M. P.; Dardik, A.; Hibino, N.; Roh, J. D.; Nelson, G. N.; Papademitris, X.; Shinoka, T. Tissue-Engineered Vascular Grafts Demonstrate Evidence of Growth and Development When Implanted in a Juvenile Animal Model. *Ann. Surg.* **2008**, *248* (3), 370–376.

(23) Hoerstrup, S. P.; Cummings, I.; Lachat, M.; Schoen, F. J.; Jenni, R.; Leschka, S.; Neuenschwander, S.; Schmidt, D.; Mol, A.; Günter, C.; et al. Functional Growth in Tissue-Engineered Living, Vascular Grafts: Follow-up at 100 Weeks in a Large Animal Model. *Circulation* **2006**, *114* (SUPPL. 1), 159–166.

(24) Matsumura, G.; Ishihara, Y.; Miyagawa-Tomita, S.; Ikada, Y.; Matsuda, S.; Kurosawa, H.;

Shin'oka, T. Evaluation of Tissue-Engineered Vascular Autografts. *Tissue Eng.* **2006**, *12* (11), 3075–3083.

(25) Dahl, S. L. M.; Kypson, A. P.; Lawson, J. H.; Blum, J. L.; Strader, J. T.; Li, Y.; Manson, R. J.; Tente, W. E.; DiBernardo, L.; Hensley, M. T.; et al. Readily Available Tissue-Engineered Vascular Grafts. *Sci. Transl. Med.* **2011**, *3* (68).

(26) Boudjemline, Y.; Laborde, F.; Pineau, E.; Mollet, A.; Abadir, S.; Borenstein, N.; Behr, L.; Bonhoeffer, P. Expandable Right Ventricular-to-Pulmonary Artery Conduit: An Animal Study. *Pediatr. Res.* **2006**, *59* (6), 773–777.

(27) Miyazaki, T.; Yamagishi, M.; Maeda, Y.; Yamamoto, Y.; Taniguchi, S.; Sasaki, Y.; Yaku, H. Expanded Polytetrafluoroethylene Conduits and Patches with Bulging Sinuses and Fan-Shaped Valves in Right Ventricular Outflow Tract Reconstruction: Multicenter Study in Japan. *J. Thorac. Cardiovasc. Surg.* **2011**, *142* (5), 1122–1129.

(28) Ugaki, S.; Rutledge, J.; Aklabi, M. Al; Ross, D. B.; Adatia, I.; Rebeyka, I. M. An Increased Incidence of Conduit Endocarditis in Patients Receiving Bovine Jugular Vein Grafts Compared to Cryopreserved Homograft for Right Ventricular Outflow Reconstruction. *Ann. Thorac. Surg.* **2015**, *99* (1), 140–146.

(29) Carrabba, M.; Madeddu, P. Current Strategies for the Manufacture of Small Size Tissue Engineering Vascular Grafts. *Front. Bioeng. Biotechnol.* **2018**, *6* (APR), 1–12.

(30) Shin'oka, T.; Matsumura, G.; Hibino, N.; Naito, Y.; Watanabe, M.; Konuma, T.; Sakamoto, T.; Nagatsu, M.; Kurosawa, H. Midterm Clinical Result of Tissue-Engineered Vascular Autografts Seeded with Autologous Bone Marrow Cells. *J. Thorac. Cardiovasc. Surg.* **2005**, *129* (6).

(31) Patterson, J. T.; Gilliland, T.; Maxfield, M. W.; Church, S.; Shinoka, T.; Breuer, C. K.

Tissue-Engineered Vascular Grafts for Use in the Treatment of Congenital Heart Disease: From the Bench to the Clinic and Back Again. **2013**, *7* (3), 409–419.

(32) O'Laughlin, M. P.; Slack, M. C.; Grifka, R. G.; Perry, S. B.; Lock, J. E.; Mullins, C. E. Implantation and Intermediate-Term Follow-up of Stents in Congenital Heart Disease. *Circulation* **1993**, *88* (2), 605–614.

(33) Cheung, Y. F.; Sanatani, S.; Leung, M. P.; Human, D. G.; Chau, A. K. T.; Culham, J. A. G. Early and Intermediate-Term Complications of Self-Expanding Stents Limits Its Potential Application in Children with Congenital Heart Disease. *J. Am. Coll. Cardiol.* **2000**, *35* (4), 1007–1015.

(34) McElhinney, D. B.; Marshall, A. C.; Schievano, S. Fracture of Cardiovascular Stents in Patients with Congenital Heart Disease. *Circ. Cardiovasc. Interv.* **2013**, *6* (5), 575–585.

(35) Peters, B.; Ewert, P.; Berger, F. The Role of Stents in the Treatment of Congenital Heart Disease: Current Status and Future Perspectives. *Ann. Pediatr. Cardiol.* **2009**, *2* (1), 3–23.

(36) Petrini, L.; Migliavacca, F. Biomedical Applications of Shape Memory Alloys. *J. Metall.* **2011**, *2011* (Figure 1), 1–15.

(37) Kirillova, A.; Ionov, L. Shape-Changing Polymers for Biomedical Applications. *J. Mater. Chem. B* **2019**, *7* (10), 1597–1624.

(38) Bisoyi, H. K.; Li, Q. Light-Driven Liquid Crystalline Materials: From Photo-Induced Phase Transitions and Property Modulations to Applications. *Chem. Rev.* **2016**, *116* (24), 15089–15166.

(39) Ionov, L. 4D Biofabrication: Materials, Methods, and Applications. *Adv. Healthc. Mater.* **2018**, *7* (17), 1–14.

(40) Yakacki, C. M.; Shandas, R.; Lanning, C.; Rech, B.; Eckstein, A.; Gall, K. Unconstrained

Recovery Characterization of Shape-Memory Polymer Networks for Cardiovascular Applications. *Biomaterials* **2007**, *28* (14), 2255–2263.

(41) Kwag, H. R.; Cho, J. H.; Park, S. Y.; Park, J.; Gracias, D. H. Self-Folding Nanostructures with Imprint Patterned Surfaces (SNIPS). *Faraday Discuss.* **2016**, *191*, 61–71.

(42) Yu, J.; Xia, H.; Teramoto, A.; Ni, Q. Q. Fabrication and Characterization of Shape Memory Polyurethane Porous Scaffold for Bone Tissue Engineering. *J. Biomed. Mater. Res. - Part A* **2017**, *105* (4), 1132–1137.

(43) Neffe, A. T.; Hanh, B. D.; Steuer, S.; Lendlein, A. Polymer Networks Combining Controlled Drug Release, Biodegradation, and Shape Memory Capability. *Adv. Mater.* **2009**, *21* (32–33), 3394–3398.

(44) Huang, Y.; Tong, D.; Zhu, S.; Wu, L.; Mao, Q.; Ibrahim, Z.; Lee, W. P. A.; Brandacher, G.; Kang, J. U. Evaluation of Microvascular Anastomosis Using Real-Time, Ultra-High-Resolution, Fourier Domain Doppler Optical Coherence Tomography. *Plast. Reconstr. Surg.* **2015**, *135* (4), 711e-720e.

(45) Huang, Y.; Ibrahim, Z.; Tong, D.; Zhu, S.; Mao, Q.; Pang, J.; Andrew Lee, W. P.; Brandacher, G.; Kang, J. U. Microvascular Anastomosis Guidance and Evaluation Using Real-Time Three-Dimensional Fourier-Domain Doppler Optical Coherence Tomography. *J. Biomed. Opt.* **2013**, *18* (11), 111404.

(46) MacDonald, J. D. Learning to Perform Microvascular Anastomosis. *Skull Base* **2005**, *15* (3), 229–240.

(47) McLaughlin, K.; Yvonne, T. Aortocoronary Saphenous Vein Graft Disease Pathogenesis, Predisposition, and Prevention. *Reggio Emilia Encount.* **2018**, 11–20.

(48) Vokrri, L.; Krasniqi, X.; Qavdarbasha, A.; Hyseni, N.; Cinquin, P.; Porcu, P.; Sessa, C. The

Vascular Connector, Design of a New Device for Sutureless Vascular Anastomosis. *Ann. Surg. Innov. Res.* **2014**, *8* (8), 1–7.

(49) Saegusa, N.; Sarukawa, S.; Ohta, K.; Takamatsu, K.; Watanabe, M.; Sugino, T.; Nakagawa, M.; Akiyama, Y.; Kusuhara, M.; Kishi, K.; et al. Sutureless Microvascular Anastomosis Assisted by an Expandable Shape-Memory Alloy Stent. *PLoS One* **2017**, *12* (7), 1–15.

(50) Chang, E. I.; Galvez, M. G.; Glotzbach, J. P.; Hamou, C. D.; El-Ftesi, S.; Rappleye, C. T.; Sommer, K. M.; Rajadas, J.; Abilez, O. J.; Fuller, G. G.; et al. Vascular Anastomosis Using Controlled Phase Transitions in Poloxamer Gels. *Nat. Med.* **2011**, *17* (9), 1147–1152.

(51) Ravi, S.; Chaikof, E. L. Biomaterials for Vascular Tissue Engineering. *Regen. Med.* **2010**, *5* (1), 107–120.

(52) Thomas, V.; Jayabalan, M. A New Generation of High Flex Life Polyurethane Urea for Polymer Heart Valve - Studies on in Vivo Biocompatibility and Biodurability. *J. Biomed. Mater. Res. - Part A* **2009**, *89* (1), 192–205.

(53) Bachtiar, E. O.; Erol, O.; Millrod, M.; Tao, R.; Gracias, D. H.; Romer, L. H.; Kang, S. H. 3D Printing and Characterization of a Soft and Biostable Elastomer with High Flexibility and Strength for Biomedical Applications. *J. Mech. Behav. Biomed. Mater.* **2020**, *104* (January), 103649.

(54) Gasparotti, E.; Vignali, E.; Losi, P.; Scatto, M.; Fanni, B. M.; Soldani, G.; Landini, L.; Positano, V.; Celi, S. A 3D Printed Melt-Compounded Antibiotic Loaded Thermoplastic Polyurethane Heart Valve Ring Design: An Integrated Framework of Experimental Material Tests and Numerical Simulations. *Int. J. Polym. Mater. Polym. Biomater.* **2019**, *68* (1–3), 1–10.

(55) van Gurp, M.; Palmen, J. Time-Temperature Superposition for Polymeric Blends. *J Rheol*

Bull **1998**, *65*, 5–8.

(56) Wu, C.; Honarmand, A. R.; Schnell, S.; Kuhn, R.; Schoeneman, S. E.; Ansari, S. A.; Carr, J.; Markl, M.; Shaibani, A. Age-Related Changes of Normal Cerebral and Cardiac Blood Flow in Children and Adults Aged 7 Months to 61 Years. *J. Am. Heart Assoc.* **2016**, *5* (1), 1–13.

(57) Pinsky, M. R. The Right Ventricle: Interaction with the Pulmonary Circulation. *Crit. Care* **2016**, *20* (1), 1–9.

(58) Alexi-Meskishvili, V.; Ovroutski, S.; Ewert, P.; Dähnert, I.; Berger, F.; Lange, P. E.; Hetzer, R. Optimal Conduit Size for Extracardiac Fontan Operation. *Eur. J. Cardio-thoracic Surg.* **2000**, *18* (6), 690–695.

(59) Liebermann --- Meffert, D. Anatomy and Embryology of the Esophagus. In *Barrett's Esophagus*; Tilanus, H. W., Attwood, S. E. A., Eds.; Springer Netherlands: Dordrecht, 2001; pp 17–30.

(60) Pang, C.; Kim, T. Il; Bae, W. G.; Kang, D.; Kim, S. M.; Suh, K. Y. Bioinspired Reversible Interlocker Using Regularly Arrayed High Aspect-Ratio Polymer Fibers. *Adv. Mater.* **2012**, *24* (4), 475–479.

(61) Toy, S. M.; Melbin, J.; Noordergraaf, A. Reduced Models of Arterial Systems. *IEEE Trans. Biomed. Eng.* **1985**, *BME-32* (2), 174–176.

(62) Dur, O.; Lara, M.; Arnold, D.; Vandenberghe, S.; Keller, B. B.; Degroff, C.; Pekkan, K. Pulsatile in Vitro Simulation of the Pediatric Univentricular Circulation for Evaluation of Cardiopulmonary Assist Scenarios. *Artif. Organs* **2009**, *33* (11), 967–976.

(63) Loneker, A. E.; Luketich, S. K.; Bernstein, D.; Kalra, A.; Nugent, A. W.; D'Amore, A.; Faulk, D. M. Mechanical and Microstructural Analysis of a Radially Expandable Vascular

Conduit for Neonatal and Pediatric Cardiovascular Surgery. *J. Biomed. Mater. Res. - Part B Appl. Biomater.* **2018**, *106* (2), 659–671.

(64) Dur, O.; Yoshida, M.; Manor, P.; Mayfield, A.; Wearden, P. D.; Morell, V. O.; Pekkan, K. In Vitro Evaluation of Right Ventricular Outflow Tract Reconstruction with Bicuspid Valved Polytetrafluoroethylene Conduit. *Artif. Organs* **2010**, *34* (11), 1010–1016.

(65) Abbott, W. M.; Megerman, J.; Hasson, J. E.; L'Italien, G.; Warnock, D. F. Effect of Compliance Mismatch on Vascular Graft Patency. *J. Vasc. Surg.* **1987**, *5* (2), 376–382.

(66) Tai, N. R.; Salacinski, H. J.; Edwards, A.; Hamilton, G.; Seifalian, A. M. Compliance Properties of Conduits Used in Vascular Reconstruction. *Br. J. Surg.* **2000**, *87* (11), 1516–1524.

(67) Mohammadi, S.; Belli, E.; Martinovic, I.; Houyel, L.; Capderou, A.; Petit, J.; Planché, C.; Serraf, A. Surgery for Right Ventricle to Pulmonary Artery Conduit Obstruction: Risk Factors for Further Reoperation. *Eur. J. Cardio-thoracic Surg.* **2005**, *28* (2), 217–222.

(68) Fleming, S.; Thompson, M.; Stevens, R.; Heneghan, C.; Plüddemann, A.; Maconochie, I.; Tarassenko, L.; Mant, D. Normal Ranges of Heart Rate and Respiratory Rate in Children from Birth to 18 Years of Age - Supplementary Webappendix. *Lancet* **2011**, *6736* (10), 1011–1018.

(69) Cattermole, G. N.; Leung, P. Y. M.; Ho, G. Y. L.; Lau, P. W. S.; Chan, C. P. Y.; Chan, S. S. W.; Smith, B. E.; Graham, C. A.; Rainer, T. H. The Normal Ranges of Cardiovascular Parameters Measured Using the Ultrasonic Cardiac Output Monitor. *Physiol. Rep.* **2017**, *5* (6), 1–9.

(70) Elliott, M. B.; Ginn, B.; Fukunishi, T.; Bedja, D.; Suresh, A.; Chen, T.; Inoue, T.; Dietz, H. C.; Santhanam, L.; Mao, H. Q.; et al. Regenerative and Durable Small-Diameter Graft as an

Arterial Conduit. *Proc. Natl. Acad. Sci. U. S. A.* **2019**, *116* (26), 12710–12719.

(71) Klarhöfer, M.; Csapo, B.; Balassy, C.; Szeles, J. C.; Moser, E. High-Resolution Blood Flow Velocity Measurements in the Human Finger. *Magn. Reson. Med.* **2001**, *45* (4), 716–719.

(72) Xu, L.-C.; Bauer, J. W.; Siedlecki, C. A. Proteins, Platelets, and Blood Coagulation at Biomaterial Interfaces. *Colloids Surfaces B Biointerfaces* **2014**, *124*, 49–68.

(73) Wong, T.-S.; Kang, S. H.; Tang, S. K. Y.; Smythe, E. J.; Hatton, B. D.; Grinthal, A.; Aizenberg, J. Bioinspired Self-Repairing Slippery Surfaces with Pressure-Stable Omniphobicity. *Nature* **2011**, *477* (7365), 443–447.

Biographical Statement

Runhan Tao was born in Zhangjiagang, China on Aug. 21st, 1997. She received her bachelor's degree in Biophysics from Nanjing University, China in 2018. She then enrolled in the Biomedical Engineering Department as a master student at Johns Hopkins University and will continue to work as a research assistant in Professor Sung Hoon Kang's lab starting from June 2020. Her research focuses on additive manufacturing and biomedical devices development.